Title

Effective mechanical potential of cell–cell interaction explains basic structures of three-dimensional morphogenesis

Short title

Effective potential of cell–cell interaction for morphogenesis

Authors

Hiroshi Koyama[1,2,*], Hisashi Okumura[2,3,4], Atsushi M. Ito[5], Tetsuhisa Otani[2,6], Kazuyuki Nakamura[7,8], Kagayaki Kato[2,9,10], and Toshihiko Fujimori[1,2]

[1]Division of Embryology, National Institute for Basic Biology, 5-1 Higashiyama, Myodaiji, Okazaki, Aichi 444-8787, Japan

[2]SOKENDAI (The Graduate University for Advanced Studies), Hayama, Kanagawa 240-0193, Japan

[3]Biomolecular Dynamics Simulation Group, Exploratory Research Center on Life and Living Systems (ExCELLS), National Institutes of Natural Sciences, 5-1 Higashiyama, Myodaiji, Okazaki, Aichi 444-8787, Japan

[4]Institute for Molecular Science, National Institutes of Natural Sciences, 5-1 Higashiyama, Myodaiji, Okazaki, Aichi 444-8787, Japan

[5]Department of Helical Plasma Research, National Institute for Fusion Science, National Institutes of Natural Sciences, 322-6 Oroshi-cho, Toki, Gifu 509-5292, Japan

[6]Division of Cell Structure, National Institute for Physiological Sciences, 5-1 Higashiyama, Myodaiji, Okazaki, Aichi 444-8787, Japan

[7]School of Interdisciplinary Mathematical Sciences, Meiji University, 4-21-1 Nakano, Nakano-ku, Tokyo 164-8525, Japan

[8]JST, PRESTO, 4-1-8 Honcho, Kawaguchi, Saitama 332-0012, Japan

[9]Bioimage Informatics Group, Exploratory Research Center on Life and Living Systems (ExCELLS), National Institutes of Natural Sciences, 38 Nishigonaka, Myodaiji, Okazaki, Aichi 444-8585, Japan

[10]Laboratory of biological diversity, National Institute for Basic Biology, 38 Nishigonaka, Myodaiji, Okazaki, Aichi 444-8585, Japan

*Correspondence: Hiroshi Koyama

Division of Embryology, National Institute for Basic Biology, 5-1 Higashiyama, Myodaiji, Okazaki, Aichi 444-8787, Japan

Phone: +81 564 59 5862,

hkoyama@nibb.ac.jp.

Author contribution

H.K. designed the work, H.K., A.M.I., and H.O. contributed to the conception. H.K. and T.F. designed experiments, T.O. provided experimental materials, and H.K. performed experiments and image processing. H.K. and H.O. designed models, H.K. developed computational algorithms, and H.K. and K.N. statistically analyzed the data. H.K., T.O., H.O., A.M.I., K.N., K.K., and T.F. wrote the manuscript, and all authors contributed to the interpretation of the results.

Conflicts of interest

The authors declare no competing financial interests.

Keywords

effective potential of cell–cell interaction, approximated multicellular model, morphological diversity, mechanics, emergent property of multicellular system, mouse pre-implantation embryo

This PDF file includes:

- Main text
- Figure 1 to 14
- Table 1
- Supplementary information (text and supplementary Figures)

Abstract

Mechanical forces of cell–cell interactions are critical for the emergence of diverse three-dimensional morphologies of multicellular organisms. Live measurements of the forces have been difficult due to technical limitations. Here, we developed a framework for inferring and modeling mechanical forces of cell–cell interactions. First, by analogy to coarse-grained models in molecular and colloidal sciences, cells were approximated as spherical particles, where the mean forces (i.e. effective forces) of pairwise cell–cell interactions were considered. Then, the forces were statistically inferred from cell tracking data, and subsequently, we successfully detected effective mechanical potentials of cell–cell interactions as a function of the cell–cell distances in epithelial cells, blastomeres, etc. Through perturbation experiments, we found that quantitative differences in the potentials reproduce morphological features in the mouse and *C. elegans* early embryos, including compaction and cavitation. In conclusion, effective potential is a measurable approximated parameter describing three-dimensional morphogenesis.

Introduction

In multicellular living systems, various three-dimensional morphologies are emerged, which is thought to be primarily dependent on the mechanical properties of the constituent cells (1–5). To understand the mechanisms of morphogenesis in large tissues including embryos, organoids, etc., predictable mathematical models are required to be developed. Multicellular systems are of many degrees of freedom. For instance, mechanical interactions among cells are provided from adhesive forces and cell surface tensions (Fig. 1A-i) (4), while there are non-cellular structures such as extracellular matrices and liquid cavities, all of which contributes to cell behaviors. Quantitative and spatiotemporal measurements of their related mechanical forces are required for developing predictable models, but are still highly challenging. Another possible solution is to develop approximated models with low degrees of freedom. This idea is analogous to molecular sciences where models used for molecular dynamics simulations are approximation of models based on quantum mechanics.

Here we explain typical examples of approximation and then present our strategy later. In two isolated cells as a simplest situation (Fig. 1A-i), because cell–cell adhesive forces reduce cell–cell distances (Fig. 1A-ii, “Attractive”), the adhesive forces may be approximated as distance-dependent attractive forces (Fig. 1A-iii, “attractive force”)(6–

101 8). Conversely, excluded volume effect of cells increases cell-cell distances (Fig. 1A-ii,
102 "Repulsive"), corresponding to repulsive forces (Fig. 1A-iii, "repulsive force"). In
103 consequence, the summation of these attractive and repulsive forces provides a distance–
104 force curve (Fig. 1A-iii), which can be written as a distance–potential energy curve (Fig.
105 1A-iv). From the profiles of these curves, we can speculate various properties of the
106 particles and of the interactions (e.g. the distance at the potential minimum corresponds
107 to the mean diameter of the particles.) (Fig. 1A-iii and -iv). Such pairwise potential of
108 cell-cell interactions is conceptually well recognized (6–15), and various profiles of the
109 potentials have been assumed in theoretical studies for multicellular systems (e.g. hard-
110 or soft-core potentials etc.) (8, 12, 16). In experiments, adhesive forces between two
111 isolated cells have been measured (i.e. forces required to dissociate one cell from the
112 other) (4, 17). However, quantitative profiles of the potentials have neither been measured
113 nor inferred, though such profiles would be critical for cell behaviors. In addition, this
114 approximation is analogous to non-living matters such as atoms, molecules, and colloids:
115 although the interactions among these matters are determined by electron clouds (i.e.
116 quantum state) which have complex shapes, approximation as pairwise potentials is
117 succeeded and is very useful for simulating large systems (18).

118 In real tissues, the situations are more complicated. For instance, cell shapes can

be far from spherical shapes in contrast to isolated cells (Fig. 1B-i). Apico-basal polarity is linked to biased localization of cell–cell adhesion proteins such as cadherins, leading to directional differences in cell–cell interaction forces (1, 2, 19). Moreover, the apico-basal polarity cannot be defined in isolated cells but can be in epithelial cell sheets in the relationship among surrounding cells (i.e. many-body effect), resulting in no adhesive capabilities on the apical and basal surfaces. However, whether pairwise potentials can be defined and experimentally measurable in real tissues remains to be addressed (Fig. 1B-ii). By contrast, modeling of polarized or non-spherical objects have been performed in atomic and molecular sciences (Fig. 1B-iii); even in the case of polarized or non-spherical molecules including water and amino acids, pairwise potentials have been sometimes defined, and these approximation models (i.e. coarse-grained models) have been succeeded to explain overall behaviors of the systems with a trade-off of microscopic accuracy (18).

To measure or infer pairwise potentials in real tissues, we were inspired by atomic and molecular sciences where inferences of potentials among these matters are a central issue. In the fields, one strategy is usage of potential energy of a whole system calculated on the basis of quantum chemistry. Then, pairwise potentials of the matters are searched for so as to satisfy the value of the above potential energy. In other words, the

137 information based on quantum chemistry is used as data to be referred during inference
138 (i.e. reference data) (20). Another simpler strategy is a usage of radial distribution
139 functions (i.e. spatial information of matters) as reference data, because the functions
140 mean probability of particle positions along particle–particle distances, which can be
141 linked to potential energy (21, 22). These resultant potentials are called effective
142 potentials which are summations of effects of various microscopic components, though
143 each component does not explicitly appear.

144 In this study, we developed a method for statistically inferring effective
145 potentials of cell–cell interactions using nuclear tracking data from live imaging as
146 reference data (Fig. 1C-i and -ii): force values of cell–cell interactions are fitted to the
147 nuclear tracking data (Fig. 1C-iii). Our method was validated by using various synthetic
148 data generated by simulations. Through these analyses, we described what kind of
149 microscopic mechanical properties such as cell surface tension can be reflected into
150 effective potentials (Fig. 1C-iv). To evaluate the applicability and limitation of our
151 method, we investigated influences of non-cellular external factors such as extracellular
152 matrix. Finally, we applied our method to real multicellular systems including the *C.*
153 *elegans* and mouse embryos, and successfully detected effective potentials of cell–cell
154 interactions. Furthermore, quantitative differences in the profiles of the effective

155 potentials can describe morphologies of the embryos (Fig. 1C-iv).

156

157

158 Theory and principle for inferring effective potential

159 In this section, we explain the inference method shown in Fig. 1C.

160

161 *Particle-based cell models*

162 In our model, particles interact with each other and attractive or repulsive forces

163 (F_i) are assumed (Fig. 1C-i), where i is an identifier for particle–particle interactions. In

164 three-dimensional cellular systems with no attachment to substrates, we did not assume

165 persistent random walks which are originated from cellular traction forces on substrates

166 (23, 24).

167 The equation of particle motions is defined below. In cellular-level phenomena,

168 viscous drag force or frictional force provided by the surrounding medium or tissue is

169 dominant, as expected from the low Reynolds number; consequently, the inertial force is

170 negligible in general (3, 6, 25–27). The forces in such a system can be assumed to be

171 correlated with the velocities of the objects (3, 12, 25, 28, 29). Thus, the velocity ($V_{C|p}$)

172 of a particle is calculated by the net force ($F_{C|p}$) exerted on the particle as follows (Fig.

173 1C-i):

174 $$V_{C|p} = F_{C|p} / \gamma \qquad \text{(Eq. 1)},$$

175 where p is an identifier for particles and γ is the coefficient of viscous drag and frictional

176 forces. $F_{C|p}$ is the summation of cell–cell interaction forces exerted on the pth particle. We
177 assumed the simplest situation, i.e., γ is constant (=1.0). Thus, by giving the values of F_i
178 from, for instance, a distance–potential curve, a simulation can run.
179
180 *Data acquisition of time series of cell positions*
181 To define cell positions, we focused on nuclei, because they are most easily
182 imaged by microscopy (Fig. 1C-ii) in a wide range of organisms from *C. elegans* to
183 mammals, and these data are accumulating (30–34). We utilized publicly available
184 nuclear tracking data of a developing embryo of *C. elegans* (30); nuclear tracking data of
185 developing mouse embryos and Madin-Darby canine kidney (MDCK) cultured cells
186 derived from dog kidney epithelium were obtained in this study.
187
188 *Development of method for inferring effective potentials/forces of cell-cell interaction*
189 In the case of ions, molecules, etc., radial distribution functions are often used to
190 infer the effective potentials of their interactions (21, 22). This method is simple, but is
191 only applicable to thermodynamically equilibrium systems because this function reflects
192 the effective potentials under equilibrium states. Therefore, this method is not suitable for
193 non-equilibrium systems, including morphogenetic events. To infer the effective

194 potentials in non-equilibrium systems, we fitted the particle-based cell model to the time
195 series of nuclear positions, where the fitting parameters are forces between all pairs of
196 cell–cell interactions for each time frame. We systematically searched for the values of
197 the effective forces between all pairs of cell–cell interactions that minimized the
198 differences (i.e. corresponding to least squares) between the particle positions in the
199 simulations and the *in vivo* nuclear positions. The differences (G_{xyz}) to be minimized are
200 defined as follows.

201 $$G_{xyz} = \sum_{t=1}^{T} \sum_{p=1}^{P(t)} \frac{\left\{x_p(t) - x_p^{\mathrm{ref}}(t)\right\}^2 + \left\{y_p(t) - y_p^{\mathrm{ref}}(t)\right\}^2 + \left\{z_p(t) - z_p^{\mathrm{ref}}(t)\right\}^2}{\Delta t}$$

202 (Eq. 2)

203 Here, p is an identifier for particles, t is an identifier for time frames, and Δt is
204 the time interval between the time frames. T is the total time frame, and $P(t)$ is the number
205 of particles at each time frame. The x, y, and z coordinates of the pth particle obtained
206 from microscopic images are x_p^{ref}, y_p^{ref}, and z_p^{ref}; ref means reference. The coordinates of
207 the simulations are x_p, y_p, and z_p. Note that, because γ was assumed to be constant in
208 Equation 1, we can only infer relative but not absolute values of effective forces.

209 To determine whether our method can correctly infer effective forces, we applied
210 it to synthetic data generated by simulations under given potentials of particle–particle
211 interactions, and examined whether the inferred effective forces were consistent with the

212 given potentials. Unfortunately, Equation 2 did not work well, and therefore, we tried to

213 incorporate various additional constraints into Equation 2. We found that the following

214 cost function worked well: the function was set so that force values approach zero at long

215 distant regions of cell–cell interactions as defined below:

216 $$G = G_{xyz} + G_{F_0} \qquad (G_{F_0} = \omega_{F_0} \sum_{t=1}^{T} \sum_{i=1}^{I(t)} \psi(D_i) F_i^2 \Delta t) \qquad \text{(Eq. 3)},$$

217 where $I(t)$ is the total number of the cell–cell interactions for each time frame, D_i is the

218 cell–cell distance of the ith interaction, and ω_{F_0} is a coefficient for determining the

219 relative contribution of the second term to G. $\Psi(D_i)$ is a distance-dependent weight that

220 exponentially increases and eventually becomes extremely large (Fig. S1A-iii). We show

221 validations of this cost function in the next sections. Detailed principles, rationale, and

222 procedures are described in SI (Section 4).

223

224 Results

225 *Systematic validation of inference method using simulation data*

226 We systematically validated our inference method using simulation data. We

227 used the Lenard–Jones (LJ) potential as a test case of the given potentials (Fig. 2A-i), and

228 generated simulation data under LJ potential, to which we applied our inference method.

229 Importantly, we assumed cell-intrinsic mechanical activities that were introduced as

230 fluctuations of the forces relative to the LJ potential (Fig. 2A-i, “fluctuation (% of LJ)”),
231 because the cells rapidly stop movements without such activities.

232 In Fig. 2A-i, the particles were initially scattered to some extent, and then
233 assembled. The inferred effective forces for each pair of particles for each time frame
234 were plotted against particle–particle distances (Fig. 2A-ii), and by calculating binned
235 averages, we obtained distance–force (DF) curves (Fig 2A-ii, yellow). In the absence of
236 the fluctuations, the data points were located around the DF curve (SD = 0%), and the DF
237 curve showed a similar profile to that from the LJ potential (Fig. 2A-iii, LJ vs. 0%). In
238 the presence of the fluctuations (SD = 100 or 1,000%), although the data points were
239 widely distributed (Fig. 2A-ii), the resultant DF curves were equivalent to that of the LJ
240 potential and of that under SD = 0% (Fig. 2A-iii). These results suggest that our method
241 is correctly applicable for assembling process even under large fluctuations of the forces.

242 In Fig. 2B-i, effective DF curves were inferred in systems under steady states
243 where particles continuously moved due to the force fluctuations (SD = 1,000%). The
244 inferred DF curves showed an almost similar profile to that of the LJ potential (Fig. 2B-
245 ii, sampling interval = 1min), but increased sampling intervals caused inconsistency with
246 the LJ potential (sampling interval = 5 min).

247 In Fig. 2C-i, effective DF curves were inferred in systems with cell proliferation

where cell numbers were increased from 38 to 47. The inferred DF curves showed a similar profile to that of the LJ potential (Fig. 2C-ii), and the influence of the sampling interval was similar to Fig. 2B.

These results suggest that our method can correctly infer the forces of cell–cell interactions even under large cell-intrinsic fluctuations. Note that long sampling intervals cause incorrectness of the inference in practice.

Applicability of inference method to epithelial cells

Next, we investigated the applicability of our inference method to epithelial cells. In epithelial cells, both cell–cell adhesive forces and cell surface tensions are exerted on the cell–cell junctions in a similar manner to the isolated two cell systems in Fig. 1A-i. Therefore, we expected that attractive and repulsive forces could describe epithelial cell–cell interactions. On the other hand, due to the tight packing of cells, potentials other than pairwise potentials are defined in the relationship among more than 2 cells, called many-body effects: in a standard mathematical model for epithelia (i.e. vertex model), many-body effects are assumed (35). If such many-body effects were dominant in epithelial cells, the relationships such as between cell–cell adhesive forces and attractive forces would disappear. To test whether attractive forces are detected in epithelial cells, we

applied our inference method to synthetic cell tracking data generated by a vertex model.

We adopted a simplest vertex model where cell–cell adhesive forces and cell surface tensions are assumed to be exerted on cell–cell junctions (Fig. 3A) (36). The adhesive forces and surface tensions function to expand and shrink the lengths of cell–cell junctions, respectively. Similar to the particle model in Fig, 2, fluctuations of forces were introduced to cell–cell junction tensions (Fig. 3A); without the fluctuations, cells rapidly stop their movements. The area elasticity reflects excluded volume effect of cells. This elasticity also contains many-body effect, because the forces are determined by all contacting cells (>2 cells) for each cell. We performed simulations with several tens of cells (Fig. 3A, “Simulation”) and obtained cell tracking data.

Fig. 3B-i shows the plots of inferred forces against cell–cell distances. In the absence of the fluctuations of tensions (0%), the distribution of the data points was not so diverged, and a DF curve was detected (Fig. 3B-i, binned average, and 3B-ii) which exhibited a typical profile with a peak of the attractive force. In the presence of the fluctuations, the distributions became wider, but the DF curves were detected whose profiles were equivalent to that without the fluctuations (Fig. 3B-ii).

Next, we examined whether microscopic features of epithelial cells were reflected into the effective DF curves. We performed simulations under various values of

284 the cell–cell adhesive forces (Fig. 3C-i). The inferred DF curves are shown in Fig. 3C-ii,
285 whose profiles are quantitatively evaluated in Fig. 3C-iii. The absolute values of the
286 maximum attractive forces were positively correlated with the cell–cell adhesive forces
287 (Fig. 3C-iii, left panel), and the distances at the maximum attractive forces were
288 negatively correlated (Fig. 3C-iii, right panel). These results are consistent with the case
289 in the isolated two cell systems. We also evaluated the effect of the cell surface tensions,
290 and found that the effect on the maximum attractive forces was opposite to the cell–cell
291 adhesive forces (Fig. 3D-i and 3D-ii). These results indicate that the effects of the
292 microscopic features of the cells are conserved among epithelial cells and isolated two
293 cell systems.

294 Finally, we evaluated the effect of the area elasticity. Under large area elasticity,
295 one expectation is that the slope of the repulsive region in the DF curve becomes steeper
296 due to its elasticity, and another expectation is that the typical profiles of DF curves
297 disappear due to its many-body effect. The inferred effective DF curves and their
298 quantitative evaluations are shown in Fig. 3E-i and 3E-ii. The typical profiles of DF
299 curves such as the peak of the attractive forces were clearly detected even under larger
300 area elasticities. The profiles of the repulsive regions were not obtained in most of the
301 conditions, though the slope under the area elasticity = 10.0 was steepest.

In summary, effective DF curves are detectable in epithelial cells, and the cell–cell adhesive forces and cell surface tensions are correctly reflected into the DF curves. These results suggest that particle models with pairwise potentials can be approximated models for epithelial cells.

Cell growth is effectively repulsive

Cell growth (i.e. cell volume increase) is an important parameter for cell behaviors and homeostasis in multicellular systems: cell growth increases pressure in multicellular systems, leading to contact inhibition of growth, delamination in epithelial sheets, and apoptosis (37–39). Under increased pressure, cells push/repel each other. In other words, the intrinsic attractive forces between cells can be effectively cancelled due to cell growth. To test this hypothesis, we used a mathematical model considering cell growth. A well-known cell growth model is shown in Fig. 4-i where one cell is modeled as two particles and the growth is described by the repulsive force between the two particles (10, 29, 37). When the distance between the two particles reaches a critical value, cell division occurs. Note that particle–particle interactions between different cells were implemented by the LJ potential (Fig. 4-i, “LJ”).

We performed simulations and inferred effective DF curves between cells (Fig.

320 4-i, “DF curve” between the orange cells). When the cell growth coefficient *B* was set to
321 be larger, cell number was increased (Fig. 4-ii). Fig. 4-iii shows the inferred effective DF
322 curves and Fig. 4-iv is their quantitative comparisons. The maximum attractive forces
323 were negatively correlated with the growth forces, and eventually, the attractive
324 components were absolutely diminished (Fig. 4-iv, left panel). In addition, the distances
325 at the maximum attractive forces were not changed by the growth forces (Fig. 4-iv, right
326 panel). These results indicate that cell growth effectively decreases attractive forces of
327 cell–cell interactions.
328
329 *Three possibilities of influences of external factors*
330 In real tissues, there are various types of non-cellular external factors which
331 affect cell behaviors; extracellular matrix, egg shells, liquid cavity, etc. We investigated
332 the applicability of our inference method to such systems. We think that there are three
333 possibilities of inference results as follows. 1) External factors do not affect inference
334 results, where correct DF curves are obtained. 2) External factors spoil inference results,
335 where obtained DF curves are meaningless. 3) External factors modulate DF curves, but
336 the effects are correctly reflected into the curves. The third possibility is analogous to
337 atomic, molecular, and colloidal sciences. For instance, external pressures increase the

338 density of objects, which is reflected into the radial distribution function linked to
339 distance–potential curves (18). Another example is solvents, where hydration of particles
340 by the solvents yields energy barriers in effective distance–potential curves (22). In
341 multicellular systems, however, it has not been clarified what kind of non-cellular external
342 factors result into the above three cases. We examined effects of several external factors
343 as follows.
344
345 *Influences of external factors; cell–extracellular matrix adhesion is effectively repulsive*
346 We investigated the effect of cell–extracellular matrix (ECM) adhesion (Fig. 5A-
347 i). Spreading of cells is regulated by competition between cell–ECM and cell–cell
348 adhesions; increased forces of cell–ECM adhesions lead to the increase in apical cell area
349 in epithelial cells (Fig. 5A-i) (19, 40, 41). Because the increase in each cell area pushes
350 surrounding cells away, the cell–ECM adhesive forces would function to repulsive forces
351 of cell–cell interactions (Fig. 5A-i, "Repulsive force"). Simultaneously, increased cell
352 areas lead to increases in distances between cells, which should be reflected as a shift of
353 effective DF curves to rightward along the cell–cell distances (Fig. 5A-i, "Shift of DF
354 curve").
355 We modeled cell–ECM adhesion in the vertex model used in Fig. 3. The potential

356 energy was defined as $E_{\mathrm{ECM}}a_n$ for each cell, where E_{ECM} is the coefficient of the
357 energy. Under increased cell–ECM adhesive forces, cell areas were increased (Fig. 5A-ii,
358 E_{ECM} = 1.0). Fig. 5A-iii shows inferred effective DF curves, and Fig. 5A-iv is the
359 quantitative evaluation of the curves. As expected, the maximum attractive forces were
360 negatively correlated with the cell–ECM adhesive forces (Fig. 5A-iv, left panel), and the
361 distances at the maximum attractive forces were increased by the cell–ECM adhesive
362 forces (Fig. 5A-iv, right panel). These results suggest that the cell–ECM adhesive forces
363 can be correctly reflected into the effective DF curves.
364
365 *Influences of external factors; traction force between cell–extracellular matrix*
366 In the presence of ECM, cells possess self-migratory activities through traction
367 forces between the cells and ECM (23, 42). We examined whether traction forces
368 influence effective DF curves. We implemented traction forces in the particle model used
369 in Fig. 2. The directions of the traction forces were set to be random (Fig. 5B-i), and
370 persist during a given time period (Fig. 5B-ii, "with persistency = 50.0min"). Cell–cell
371 interaction forces were provided by the LJ potential (Fig. 5B-i, "LJ"). The value of the
372 traction forces is shown as a relative value to the maximum attractive force of the LJ
373 potential (Fig. 5B-ii, "1,000% of LJ"). Simulations were performed two-dimensionally.

374 Fig. 5B-iii shows inferred effective DF curves. In the absence of the traction
375 forces (0%), the inferred curve showed a similar profile to the given LJ potential, though
376 an inconsistency was observed at the distant region (distance = ~7μm). In the case that
377 the value of traction forces was equivalent to the attractive force of the LJ potential
378 (100%), the curve was consistent with that without the traction forces, whereas, under a
379 larger traction force (1,000%), the curve became highly repulsive. Fig. 5-iv shows effects
380 of persistency of the traction forces. Even under the large traction forces (1,000%), a DF
381 curve was consistent with that from the LJ potential if the persistency was short (left panel,
382 1.0min). In conclusion, traction forces can significantly modify effective DF curves if
383 both the force value and the persistency are large. Otherwise, correct DF curves can be
384 obtained. We speculate that this modification spoils the inference. Similar repulsive
385 profiles of DF curves were obtained in MDCK cells on substrates, which have high self-
386 migratory activities (Fig. S3A).
387
388 *Influences of external factors; egg shell has no influence on effective forces*
389 Next, we introduced spatial constraints corresponding to egg shells. The particles
390 with the LJ potential were put into cylindrical constraints (Fig. 6A-i). In longer lengths
391 of cylinders, inferred DF curves were well consistent with the DF curves from the LJ

392 potential (Fig. 6A-ii; length of cylinder ≥ 25μm). By contrast, under shorter cylinders, the
393 profiles of inferred DF curves were shifted leftward along the distance (Fig. 6B-ii; length
394 of cylinder ≤ 20μm). This shift is reasonable as follows. A snapshot of the simulation
395 under the length = 16μm is shown in Fig. 6A-ii, where the particle diameters were set to
396 be equivalent to the mean diameter of cells defined in Fig. 1A-iii. The particles were very
397 closely contacted each other so that the distances between the adjacent particles seemed
398 to be less than the diameter of the particles. Therefore, the particles were compressed.
399 Radial distribution functions under compressed conditions should also shift leftward
400 along the distance (Fig. 6A-iii, "non-compressive" vs. "compressive"), which are linked
401 to effective DF curves. Therefore, our inference method can correctively reflect the effect
402 of compression into effective DF curves. However, in cell biology, we think that the
403 compressive conditions are not physiologically relevant, because cells are essentially
404 composed of non-compressive liquid and their volumes are not changed by external
405 pressure. In conclusion, DF curves are correctly inferred under spatial constraints.
406
407 *Influences of external factors; liquid cavity is approximated as effective forces*
408 Next, we introduced cavities. Cells can generate cavities by secreting liquid, and
409 then the pressure of the cavities push the cells away (43–45). Here we implemented

expanding cavities as spatial constraints in simulations (Fig. 6B-i, the radius of the cavity is increased from 9.6 to 12.6μm), and the particles with the LJ potential move on the surfaces of the cavities. Fig. 6B-ii shows that inferred effective DF curves were not consistent with the DF curves from the LJ potential, where repulsive components were strongly detected especially at distant regions, which we call distant energy barrier (DEB).

We then examined whether this modification is meaningless or is a result of a correct reflection of the expanding cavities. By performing simulations with the expanding cavities but without the LJ potential (Fig. 6C-i), we solely extracted the influence of the expanding cavities. Fig. 6C-ii shows that the inferred DF curves were absolutely composed of repulsive components. Then, we checked the raw data where all data points were plotted on the distance–force graph. In Fig. 6D-i, "From C", a heat map of the data points is shown with binned averages (yellow) corresponding to the DF curve in Fig. 6C-ii. Interestingly, all the data points were closely located around the DF curve ("From C"), implying that the DF curve is a good approximation of the expanding cavities.

Finally, by using the above information, we examined whether the correct DF curve (i.e. LJ potential) can be reconstructed. We subtracted the DF curves of Fig. 6C from those of Fig. 6B (Fig. 6D-i, "From B – From C"). The resultant DF curves in Fig. 6D-ii were well consistent with the LJ potential under any expansion rates of the cavities.

These results suggest that the effects of the expanding cavities can be approximated as effective DF curves.

We interpret the above results as described in Fig. 6E. A cell receives forces from cell–cell interactions ("LJ") and from the pressure from the cavity, where the vector of the pressure is perpendicular to the surface of the cavity (Fig. 6E, top panel). The repulsive forces detected as cell–cell interactions in Fig. 6C are described in Fig. 6E, middle panel, and the vector of the net force is perpendicular to the surface of the cavity, if the cells are almost uniformly distributed. Therefore, the pressure from the cavity can be equivalent to the net force from the DEBs (Fig. 6E, bottom panel), leading to the successful reconstruction of the LJ potential.

We conclude that the expanding cavities can be approximated as effective potentials. Effective potentials are the summation of different components as explained in Fig. 1A-iii. External factors are also one of the components in molecular and colloidal sciences: e.g. by considering hydration of particles by solvents, effective potentials are modified so as to contain energy barriers around distant regions (21, 22), and such effective potentials have been used to simulate behaviors of the systems.

Inference of effective forces in C. elegans early embryo

446 We next investigated whether effective potential could be detected as a function
447 of cell–cell distance in three-dimensional *in vivo* systems. The nematode *C. elegans* has
448 well-defined embryogenesis: cell movements in early embryos are almost identical
449 among different individuals, and the time series of nuclear positions have been reported
450 previously (30). During early *C. elegans* embryogenesis, a fertilized egg (i.e. one cell)
451 repeatedly undergoes cell division and cell differentiation in a stiff/undeformable egg
452 shell, ultimately forming an ovoid embryo containing ~350 cells (Fig. S6A and Movie
453 S1A). The cells become smaller through cell division (46), and the total volume of the
454 embryo remains constant. Thus, the volume of each cell is reduced by a factor of 350
455 relative to the original egg, meaning that mean cell diameter is reduced by a factor of 7.
456 Because particle diameter is approximately reflected on a DF curve (Fig. 1A-iii), we
457 expected that inferred DF curves should be gradually shifted to the left side of the
458 distance–force graph throughout embryogenesis.

459 Figure 7A is a snapshot that shows nuclear positions with the cell lineage and
460 inferred effective forces where the color of the lines corresponds to the values of the
461 forces (Movie S1B). The temporal changes in the mean diameters of the cells were
462 estimated in Fig. 7B; e.g., the diameter at t (time frame) = 195 is ~28% of that at t = 16.
463 In our inference in this system, we confirmed that this inference problem has essentially

464 a unique solution (Fig. 7C).

465 We divided the whole embryogenesis into segments containing different time
466 frames, and obtained DF curves. Fig. 7D is an example of the DF curve (binned average)
467 at t = 76-115 with all data points shown as a heat map. Although the data points were
468 widely distributed similar to the previous figures (e.g., Fig. 2A and 3B), a clear DF curve
469 was detected. Fig. 7E shows the DF and DP (distance–potential) curves for each period (t
470 = 16–55, 36–75, 76–115, 116–155, and 156–195). These curves were gradually shifted
471 toward the left side (Fig. 7E), as we had theoretically expected, indicating that the inferred
472 effective potentials were quantitatively consistent with the reduction in cell volume
473 during embryogenesis. To evaluate differences in mechanical properties among the
474 periods, we normalized both the distances and potentials by the distances at the potential
475 minima (Fig. 7F). The curves were almost unchanged during the periods, suggesting that
476 the mechanical properties of cell–cell interactions are not drastically modulated during
477 the development except for the cell sizes.

478

479

480 *Inference of effective force in mouse pre-implantation embryos*

481 To further investigate whether effective forces could be obtained in three-

482 dimensional systems, we focused on mouse pre-implantation embryos, including morulae
483 at the 8-cell, compaction, and blastocyst stages (Fig. 8A, illustration). In 8-cell stage
484 embryos before compaction, cell–cell adhesion is weak, and individual cells can be easily
485 discerned (Fig. 8A, bright field). In the compaction-stage embryos composed of ~16-32
486 cells, cell–cell adhesion becomes stronger due to elevated expression of cadherin proteins
487 on cell membrane, and the cells are strongly assembled (47). The surface of the embryo
488 becomes smooth, and the embryonic shape becomes more spherical (Fig. 8A, bright field).
489 In blastocyst-stage embryos composed of >64 cells, an inner cavity is formed through
490 liquid secretion from the cells, and the embryos expand while maintaining their spherical
491 shape (43–45) (Fig. 8A, bright field and cross-section). Trophectoderm (TE) cells form a
492 single–cell-layered structure at the outermost surface of the embryo, whereas the cells of
493 the inner cell mass (ICM) were tightly assembled, forming a cluster (Fig. 8A, illustration).
494 We performed cell tracking (Fig. 8A, tracking) and inferred effective forces.

495 Fig. 8B and 8C shows the inferred effective DF and DP curves for all three stages.
496 The DF curves derived from the 8-cell and compaction stages had typical profiles, with
497 repulsive and attractive forces detected. On the other hand, the DF curves derived from
498 the blastocyst stage contained highly repulsive regions (Fig. 8B, DEB), similar to the case
499 of simulation data considering an expanding cavity (Fig. 6B). Moreover, when we

500 inhibited the cavitation by an inhibitor for Na^+/H^+ exchanger (S3226) (48), DEB was
501 diminished in the inferred potentials (Fig. S9), indicating that the cavity yielded the DEBs.
502 These results indicate that the effective DF curves experience changes in their profiles
503 during the development.
504
505 *Inference of effective distance–force curves in MDCK cyst*
506 To further test the applicability of our method to structures harboring cavities,
507 we focused on MDCK cells which can form cysts containing a cavity when cultured in
508 suspension (Fig. 9A, illustration) or in gels composed of ECM (49). To exclude adhesion
509 between the cysts and the ECM, we chose suspension conditions in which a cyst can be
510 assumed to be a mechanically isolated system. Fig. 9B and 9C show the DF and DP curves.
511 A DEB was detected in the DF curves.
512
513 *Effective potentials are capable of describing morphologies*
514 Effective DF/DP curves are the summation of the multiple components including
515 the excluded volume effect, adhesive forces, and external factors, and are useful to study
516 behaviors of systems in molecular and colloidal sciences. We evaluated whether inferred
517 effective DF curves from the *C. elegans*, mouse embryos, and MDCK cysts can reproduce

518 their morphologies. In simulations of multicellular systems, the morphologies are
519 determined by both DF curves and initial configurations, because energetic local
520 minimum states (i.e. metastable state) as well as global minimum states are meaningful.
521 To find stable states under the DF curves, we performed simulations starting from various
522 initial configurations of the particles, and the systems were relaxed.

523 From the DF curves of the *C. elegans* embryos, we observed a tendency that the
524 particles form an aggregate with an ovoid or distorted shape (Fig. 10A). These results
525 may be consistent with experimental observations: the embryonic cells can keep a cell
526 aggregate even when the eggshell is removed, and subsequent culture leads to a cell
527 aggregate with an ovoid or distorted shape, except for very early stage of development (<
528 ~20 cells) (50, 51).

529 From the DF curves of the mouse embryos, a spherical aggregate was generated
530 in the compaction stage, whereas a cavity-bearing structure was in the blastocyst stage
531 (Fig. 10B); these morphologies are consistent with the *in vivo* situations. To examine
532 whether the DEB contribute to the formation of a cavity, we artificially eliminated the
533 DEB from the DF curves, and performed a simulation. We found that no cavity was
534 generated but an aggregate was formed (Fig. 10B, "DF curve w/o DEB").

535 From the DF curve of the MDCK cysts, a cavity-bearing structure was generated

536 (Fig. 10C), and artificial elimination of the DEB led to generation of a no-cavity structure
537 but an aggregate.
538 These results suggest that all of the DF curves from the various species and
539 various embryonic stages are capable of recapitulating their basic morphologies.
540
541 *Robustness of simulation outcomes*
542 As shown above, the ovoid/distorted shape or spherical shape were generated in a manner
543 dependent on DF curves. We examined whether our inference robustly results into the
544 same simulation outcomes. During the minimization of the cost function *G*, we sampled
545 DF curves before reaching the minimum of *G*. Fig. 10D shows the DF curves for the *C.*
546 *elegans* embryo t36-75 (left panel), and their values of *G* are plotted against the maximum
547 attractive force in the DF curves (right panel); the colors in the two panels correspond
548 each other. Before reaching the minimum (a red line in left panel and a red circle in the
549 right), the DF curves exhibited some differences in their profiles. Then, simulations were
550 performed from an initial configuration which shows a cuboid shape (bottom panel,
551 "start"). For all the DF curves tested, the particles were not spherically assembled but the
552 initial cuboid shape was almost sustained. By contrast, in the case of the mouse
553 compaction stage shown in Fig. 10E, the particles were spherically assembled for all the

554 DF curves except for an intermediate sample (light blue) which shows two isolated
555 aggregates. These results suggest that simulation outcomes resulting from our inference
556 are robust, and the DF curves are sufficient to explain morphologies among different
557 tissues.
558
559 *Perturbation experiments for mouse compaction stage embryo*
560 To evaluate the predictive capability of the DF curves inferred by our method,
561 we performed perturbation experiments. In the mouse compaction stage, the cells are
562 tightly assembled to form a spherical and symmetric embryonic shape. In other words,
563 we think that there are two morphological features, 1) increase in symmetry of the
564 embryos, and 2) smoothing of the embryonic surfaces. The embryos are surrounded by
565 external structures called zona pellucida which have negligible effects on morphogenesis
566 (52). Because both E-cadherin and actomyosin are essential for the compaction process
567 (47, 53, 54), we inhibited these proteins by chemicals: EDTA (ethylenediaminetetraacetic
568 acid) for E-cadherin, cytochalasin D for F-actin, and blebbistatin for non-muscle myosin
569 II (Fig. 11A).
570 The effective DP curves were inferred under these drugs (Fig. 11B). Then, we
571 quantitatively evaluated the differences among the DP curves and found that the distances

572 at the potential minima were increased under the three inhibitors (Fig. 11C, left panel).
573 Because the distances at the potential minima are related to the mean diameters of cells
574 (Fig. 1A-iv), this result predicted that the distances between adjacent cells were increased.
575 This prediction was supported through histological observations: each cell exhibited a
576 nearly spherical shape and seemed that the cells were not so densely assembled especially
577 under the condition of EDTA compared with the no-drugs condition (Fig. 11D). The
578 embryonic and cellular shapes are schematically depicted in Figure 11E. In addition, we
579 found another quantitative difference among the DP curves, related to decay of attractive
580 forces. We measured distances at 10% energy of potential minima as relative values to
581 the distances at the potential minima, and found that the relative distances were decreased
582 under EDTA and blebbistatin (Fig. 11C, right panel). This result means that attractive
583 forces of long-range interactions were reduced under these drugs.
584
585 *Predictive capability of effective potential for mouse compaction stage embryo*
586 Simulations under the DP curves from the drugs-treated embryos were
587 performed. The cell particles were spherically or almost spherically assembled under the
588 potentials of the normal embryos or the cytochalasin D-treated embryos, respectively (Fig.
589 12A). By contrast, the cell particles were not spherically assembled under the potentials

590 of the EDTA or blebbistatin-treated embryos. All simulation data are provided in Figure
591 S18A from which representative results are shown in Fig. 12A.

592 To relate the profiles of the DP curves to morphological changes in the
593 compaction process, we first introduced two indices for the morphologies as follows.
594 Sphericity ($=(36\pi V^2)^{1/3}/S$) is essentially defined as the ratio of volume (V) to surface area
595 (S) so that the value becomes 1.0 for spheres. Shapes other than spheres show values less
596 than 1.0. Thus, both the increases in symmetry and in smoothness of surfaces contribute
597 to this index. Aspect ratio is defined as the ratio of the length of the longest axis to that of
598 the shortest axis in an ellipsoid which is fitted to an object of interest. The increase in
599 symmetry leads to that the aspect ratio becomes 1.0, and otherwise the aspect ratio shows
600 more than 1.0. The sphericities of all simulation results in Figure 12A and S18A were
601 measured, and we found that the sphericities were decreased under EDTA and blebbistatin
602 (Fig. 12B, left panel). Similarly, the aspect ratios were increased under EDTA and
603 blebbistatin (Fig. 12C, left panel).

604 We searched for parameters which can describe the sphericities or aspect ratios.
605 Among several parameters tested, the distances at potential minima measured in Figure
606 11C showed a tight relationship to the sphericities (Fig. 12B, right panel). The sphericities
607 showed an abrupt change along the x-axis. These results indicate that the sphericity is the

order parameter for the morphological transition of the compaction process and that the distance at the potential minimum is the control parameter. On the other hand, the relative distances at 10% potential minima showed a clear relationship to the aspect ratios (Fig. 12C, right panel). Thus, the morphological transitions of the compaction process are induced by the quantitative changes in the DP curves.

Modeling of distance–force curves

To comprehensively understand the effect of the differences of the DF curves on morphogenesis, we modeled the DF curves as a simple mathematical equation. To analyze the contribution of DEBs, we selected the following equation (Fig. 13A):

$$F(D) = \varepsilon(D - D_0)^{-N} \cos\left\{\frac{2\pi(D - D_0)}{\delta}\right\}, \text{ for } D > D_0 \qquad \text{(Eq. 4)}$$

Here, F is the force, D is the distance, and δ affects the wavelength of the cosine function by which DEB is also introduced (Fig. 13A, left panel, red). D_0 can transform the DF curves along D, and thus, the relative positions of DEBs to the mean diameters are changed (Fig. 13A, D_3 in red vs. blue). N is the exponent of D, affecting the decay of the DF curves along D (X-axis), and thus, the strengths of DEBs are changed (Fig. 13A, right panel). All parameters and variables related to lengths/distances were normalized by (δ/4), leading to generation of dimensionless parameters and variables such as $D_0^* = D_0 / (\delta/4)$.

This enabled us to present simulation outcomes in two-dimensional space (D_0^* and N) in a manner similar to a phase diagram (Fig. 13B) as explained in the next section.

Appropriate position and strength of DEB are essential for cavity-bearing structures

First, we examined what kind of DF curves can maintain a cavity-bearing structures. A cavity-bearing structure was set as the initial configuration (Fig. 13B, "Initial configuration"), and simulations were performed until the systems reached steady states including metastable states. Fig. 13B shows a phase diagram with representative images of the simulations, on which the regions of cavity-bearing structures were identified ("cavity" and "cavity with extra particles"). The "cavity" category absolutely depended on the DEBs, because DF curves whose DEBs were eliminated did not form the "cavity" as shown in Fig. 13C. In Fig. 13B, the "cavity" category was located around smaller N values, otherwise aggregates were formed, suggesting that the strengths of the DEBs were effective. Furthermore, larger D_0 values were required for the "cavity" category, otherwise multiple clusters were formed, suggesting that the relative positions of DEBs should be close to the mean diameters. Under a different number of particles, a similar trend was observed (Fig. S21). In addition, we found cups and tubes adjacent to the "cavity" in Fig. 13B but not in Fig. 13C, indicating that the DEBs also contribute to the

formation of these structures. The maintenance of tubes was confirmed to be dependent on DEBs (Fig. S22). Therefore, in real tissues with tubes or cups, inferred effective potentials may harbor DEBs.

Profiles of distance–force curves for describing 2D sheet, spherical/non-spherical aggregates

To further investigate the capability of DF curve, we next applied a two-dimensional (2D) sheet as the initial configuration which corresponds to a monolayered cell sheet (Fig. 14A, “Initial configuration”). Fig. 14A shows a phase diagram with representative simulation images. The 2D sheets were maintained ("sheet”), which was largely dependent on the presence of DEBs (Fig. 14A, w/ DEBs vs. 14B, w/o DEBs). We confirmed that the 2D sheets were not broken by slight positional fluctuations (Movie S4), indicating that the structures were stable. The region of the 2D sheets was located around larger values of D_0, which was a similar trend to the case of the cavity in Fig. 13.

In Fig. 14, both spherical and non-spherical aggregates were generated w/ and w/o DEBs, and smaller values of N and/or D_0 led to the spherical ones. Under smaller values of D_0, because the width (W_1) of the attractive force regions in DF curves became relatively longer to the mean diameter (D_1), the resultant increased attractive forces may

662 cause the spherical aggregates. Under smaller values of N, the potential energies (P_1)
663 derived from the attractive forces are increased, possibly leading to the spherical
664 aggregates. Unexpectedly, the cavity-bearing structures were newly generated even in the
665 absence of the DEBs (Fig. 14B) in contrast to Fig. 13.
666
667
668 Discussion
669 In this study, we developed a top-down method for statistically inferring
670 effective potentials of cell–cell interactions using cell tracking data. We then
671 demonstrated that effective potentials are detectable as a function of cell–cell distances
672 with close relations to microscopic features such as cell surface tensions in epithelial cells
673 and blastomeres. Our findings provide for the first time the experimental quantification
674 of effective potentials, which have been recognized conceptually (6, 7). Simultaneously,
675 our findings provide a rationale that particle models with effective potentials can be a
676 good approximated model for various cells, which will enable us to expand the
677 applicability of particle models to larger organs. Furthermore, effective potentials with
678 qualitative and quantitative differences in their profiles were capable of describing
679 various morphogenesis such as the compaction process in the mouse embryos, cavitations,

formation of spherical/non-spherical aggregates, etc., suggesting that effective potentials are powerful to explain the emergent properties of multicellular systems.

Effective potentials as measures of mechanical property

We showed that cell–cell adhesive force, cell surface tensions, and cell growth are reflected into effective potentials (summarized in Table 1). Moreover, inhibitions of gene function modified effective potentials (Fig. 11, S3, and S9). These facts suggest that effective potentials can be a measure for evaluating mechanical properties of systems including mutants in a non-invasive manner.

Influence of external factors on effective potentials

External factors exhibited influences on effective potential in different ways as summarized in Table 1. Moreover, expanding cavities were approximately reflected into effective potentials as DEBs, whereas higher self-migratory activities spoiled inference results. Possibly, if we could subtract the movements derived from the self-migratory activities by using the traction force microscopy (42, 55), we would correctly infer effective potentials. Simulations considering DEBs unexpectedly formed cups, tubes, and 2D sheets as well as cavities. These structures are often observed during embryogenesis,

698 morphogenesis, and organoids prior to the formation of complex tissue structures: cavity-
699 bearing structures in early embryos of various species, organoids, and cystic diseases (49,
700 56–59), cell sheets in epithelia and germ layers (41, 60–62), tubes in tubular organs (63,
701 64), cups in retina (i.e. optic cup) and murine epiblast (65, 66). Our goal is to develop a
702 framework for explaining diverse morphogenesis in a minimal model. Approximations of
703 some external factors as effective potentials of cell–cell interaction serve to reduce
704 degrees of freedom.
705
706 *Comparison of other inference methods with other models*
707 To understand morphogenetic events, mechanical states and simulations based
708 on those states are essential. Models such as vertex, Cellular Potts, and phase field models
709 are often utilized, especially for epithelial cells (3, 56, 67–69). These models successfully
710 recapitulated various morphogenetic events, including the formation of the mouse
711 blastocyst (67) and very early embryogenesis in *C.elegans* (70). However, it is still
712 challenging to measure cellular and non-cellular parameters in three-dimensional systems
713 with high spatiotemporal resolution, although high-resolution inferences of parameters
714 such as cell–cell junction tensions and stresses have been performed in two-dimensional
715 situations by fitting a vertex model to experimental observations (71, 72). In addition,

because the assumptions of the vertex model are based on epithelial cells, its application to other cells is limited including blastomeres and mesenchymal cells. On the other hand, particle models are mainly used for cell aggregates and self-propelled cells (10, 12), while some papers applied particle models to epithelial cells (11, 14, 61, 73), meaning that the applicability of particle models is expanding. Due to its simplicity of particle models (i.e. low degrees of freedom), our method can provide a framework for quantitatively connecting model parameters to *in vivo* parameters under three-dimensional situations.

Materials and methods

Details of experimental procedures, mathematical modeling, and statistical methods are described in Supplementary information.

Acknowledgement

We thank Drs. Hitoshi Niwa and Yayoi Toyooka for providing the piggy-bac plasmids and technical suggestions. We thank Drs. Jean-François Joanny, Hiroaki Takagi and Yasuhiro Inoue for critical reading of the manuscript. We thank Dr. Yoshitaka Kimori for helpful discussions. We thank Ms. Azusa Kato for supporting nuclear tracking. This work was supported by following grants: Japan Ministry of Education, Culture, Sports, Science

and Technology Grant-in-Aid for Scientific Research on Innovative Areas “Cross-talk between moving cells and microenvironment as a basis of emerging order” for H.K., the National Institutes of Natural Sciences (NINS) program for cross-disciplinary science study for H.K., a Japan Society for the Promotion of Science (JSPS) Grant-in-Aid for Young Scientists (B) for H.K. (17K15131), for Scientific Research (C) for T.O. (18K06234), and for Young Scientists (B) for T.O. (16K18544), a MEXT/JSPS Grant-in-Aid for Scientific Research on Innovative Areas for T.O. (17H05627), the Inamori Foundation for T.O., and the Takeda Science Foundation for T.O.

References

1. M. S. Steinberg, Differential adhesion in morphogenesis : a modern view. *Curr. Opin. Genet. Dev.* **17**, 1281–286 (2007).
2. C. Guillot, T. Lecuit, Mechanics of epithelial tissue homeostasis and morphogenesis. *Science (80-.).* **340**, 1185–9 (2013).
3. A. G. Fletcher, M. Osterfield, R. E. Baker, S. Y. Shvartsman, Vertex models of epithelial morphogenesis. *Biophys. J.* **106**, 2291–2304 (2014).
4. J.-L. Maître, *et al.*, Adhesion Functions in Cell Sorting by Mechanically Coupling the Cortices of Adhering Cells. *Science (80-.).* **338**, 253–256 (2012).

5. E. Bazellières, *et al.*, Control of cell–cell forces and collective cell dynamics by the intercellular adhesome. *Nat. Cell Biol.* **17**, 409–420 (2015).

6. G. Forgacs, S. A. Newman, *Biological Physics of the Developing Embryo* (Cambridge University Press, 2005).

7. M. Merkel, M. L. Manning, Using cell deformation and motion to predict forces and collective behavior in morphogenesis. *Semin. Cell Dev. Biol.* **67**, 161–169 (2017).

8. D. Drasdo, R. Kree, J. S. McCaskill, Monte Carlo approach to tissue-cell populations. *Phys. Rev. E* **52**, 6635–6657 (1995).

9. T. R. Weikl, M. Asfaw, H. Krobath, R. Bartosz, R. Lipowsky, Adhesion of membranes via receptor–ligand complexes: Domain formation, binding cooperativity, and active processes. *Soft Matter* **5**, 3213–3224 (2009).

10. J. Ranft, *et al.*, Fluidization of tissues by cell division and apoptosis. *Proc. Natl. Acad. Sci. U. S. A.* **107**, 20863–20868 (2010).

11. N. Sepúlveda, *et al.*, Collective Cell Motion in an Epithelial Sheet Can Be Quantitatively Described by a Stochastic Interacting Particle Model. *PLoS Comput. Biol.* **9**, e1002944 (2013).

12. B. Szabó, *et al.*, Phase transition in the collective migration of tissue cells:

Experiment and model. *Phys. Rev. E* **74**, 061908 (2006).

13. J. M. Belmonte, G. L. Thomas, L. G. Brunnet, R. M. C. de Almeida, H. Chate, Self-Propelled Particle Model for Cell-Sorting Phenomena. *Phys. Rev. Lett.* **100**, 248702 (2008).

14. S. B. Nissen, S. Rønhild, A. Trusina, K. Sneppen, Theoretical tool bridging cell polarities with development of robust morphologies. *Elife* **7**, e38407 (2018).

15. J. Delile, M. Herrmann, N. Peyriéras, R. Doursat, A cell-based computational model of early embryogenesis coupling mechanical behaviour and gene regulation. *Nat. Commun.* **8**, 13929 (2017).

16. M. R. D'Orsogna, Y. L. Chuang, A. L. Bertozzi, L. S. Chayes, Self-Propelled Particles with Soft-Core Interactions : Patterns , Stability , and Collapse. *Phys. Rev. Lett.* **96**, 104302 (2006).

17. J. Kashef, C. M. Franz, Quantitative methods for analyzing cell–cell adhesion in development. *Dev. Biol.* **401**, 165–174 (2015).

18. P. Atkins, J. De Paula, J. Keeler, *Atkins' Physical Chemistry*, 11th ed. (Oxford University Press, 2018).

19. J. Yong, *et al.*, Spatial distribution of cell–cell and cell–ECM adhesions regulates force balance while maintaining E-cadherin molecular tension in cell pairs. *Mol.*

Biol. Cell **26**, 2456–2465 (2015).

20. A. M. Ito, A. Takayama, S. Saito, H. Nakamura, Formation and Classification of Amorphous Carbon by Molecular Dynamics Simulation. *Jpn. J. Appl. Phys.* **52**, 01AL04 (2013).

21. B. M. Pettitt, P. J. Rossky, Alkali halides in water: Ion–solvent correlations and ion–ion potentials of mean force at infinite dilution. *J. Chem. Phys.* **84**, 5836–5844 (1986).

22. J. N. Israelachvili, *Intermolecular and Surface Forces*, 3rd ed. (Elsevier Inc., 2011).

23. S. Garcia, *et al.*, Physics of active jamming during collective cellular motion in a monolayer. *Proc. Natl. Acad. Sci. U. S. A.* **112**, 15314–15319 (2015).

24. M. Basan, J. Elgeti, E. Hannezo, W.-J. Rappel, H. Levine, Alignment of cellular motility forces with tissue flow as a mechanism for efficient wound healing. *Proc. Natl. Acad. Sci.* **110**, 2452–2459 (2013).

25. X. Li, *et al.*, On the mechanism of long-range orientational order of fibroblasts. *Proc. Natl. Acad. Sci.* **114**, 8974–8979 (2017).

26. E. Schötz, *et al.*, Quantitative differences in tissue surface tension influence zebrafish germ layer positioning. *HFSP J.* **2**, 42–56 (2008).

27. B. He, K. Doubrovinski, O. Polyakov, E. Wieschaus, Apical constriction drives tissue-scale hydrodynamic flow to mediate cell elongation. *Nature* **508**, 392–396 (2014).

28. Y. Arboleda-Estudillo, *et al.*, Movement Directionality in Collective Migration of Germ Layer Progenitors. *Curr. Biol.* **20**, 161–169 (2010).

29. M. Basan, J. Prost, J.-F. Joanny, J. Elgeti, Dissipative particle dynamics simulations for biological tissues: rheology and competition. *Phys. Biol.* **8**, 026014 (2011).

30. Z. Bao, *et al.*, Automated cell lineage tracing in Caenorhabditis elegans. *Proc. Natl. Acad. Sci. U. S. A.* **103**, 2707–2712 (2006).

31. K. McDole, *et al.*, In Toto Imaging and Reconstruction of Post-Implantation Mouse Development at the Single-Cell Level. *Cell* **175**, 859-876.e33 (2018).

32. F. Amat, P. J. Keller, Towards comprehensive cell lineage reconstructions in complex organisms using light-sheet microscopy. *Dev. Growth Differ.* **55**, 563–578 (2013).

33. K. Kyoda, *et al.*, WDDD: Worm developmental dynamics database. *Nucleic Acids Res.* **41**, D732-7 (2013).

34. Y. Kurotaki, K. Hatta, K. Nakao, Y.-I. Nabeshima, T. Fujimori, Blastocyst axis is

specified independently of early cell lineage but aligns with the ZP shape. *Science* **316**, 719–23 (2007).

35. D. Bi, X. Yang, M. C. Marchetti, M. L. Manning, Motility-driven glass and jamming transitions in biological tissues. *Phys. Rev. X* **6**, 021011 (2016).

36. M. Suzuki, *et al.*, Distinct intracellular Ca 2 + dynamics regulate apical constriction and differentially contribute to neural tube closure. *Development* **144**, 1307–1316 (2017).

37. N. Podewitz, M. Delarue, J. Elgeti, Tissue homeostasis: A tensile state. *Epl* **109**, 1–6 (2015).

38. E. Marinari, *et al.*, Live-cell delamination counterbalances epithelial growth to limit tissue overcrowding. *Nature* **484**, 542–545 (2012).

39. J. Zimmermann, B. A. Camley, W. Rappel, H. Levine, Contact inhibition of locomotion determines cell – cell and cell – substrate forces in tissues. *Proc. Natl. Acad. Sci.* (2016) https:/doi.org/10.1073/pnas.1522330113.

40. P. L. Ryan, R. A. Foty, J. Kohn, M. S. Steinberg, Tissue spreading on implantable substrates is a competitive outcome of cell–cell vs . cell–substratum adhesivity. *Proc. Natl. Acad. Sci. U. S. A.* **98**, 4323–4327 (2001).

41. C. Pérez-González, *et al.*, Active wetting of epithelial tissues. *Nat. Phys.* **15**, 79–

88 (2019).

42. K. Aoki, *et al.*, Propagating Wave of ERK Activation Orients Collective Cell Migration. *Dev. Cell* **43**, 305–317 (2017).

43. K. Moriwaki, S. Tsukita, M. Furuse, Tight junctions containing claudin 4 and 6 are essential for blastocyst formation in preimplantation mouse embryos. *Dev Biol* **312**, 509–22 (2007).

44. X. Wang, *et al.*, Characterizing Inner Pressure and Stiffness of Trophoblast and Inner Cell Mass of Blastocysts. *Biophys. J.* **115**, 2443–2450 (2018).

45. J. G. Dumortier, *et al.*, Hydraulic fracturing and active coarsening position the lumen of the mouse blastocyst. *Science (80-.).* **365**, 465–468 (2019).

46. Y. Arata, H. Takagi, Y. Sako, H. Sawa, Power law relationship between cell cycle duration and cell volume in the early embryonic development of Caenorhabditis elegans. *Front. Physiol.* **5**, 529 (2015).

47. J. C. Fierro-González, M. D. White, J. C. Silva, N. Plachta, Cadherin-dependent filopodia control preimplantation embryo compaction. *Nat. Cell Biol.* **15**, 1424–33 (2013).

48. R. Kawagishi, *et al.*, Na+/H+ exchanger-3 is involved in mouse blastocyst formation. *J. Exp. Zool. Part A Comp. Exp. Biol.* **301**, 767–775 (2004).

49. A. Z. Wang, G. K. Ojakian, W. J. Nelson, Steps in the morphogenesis of a polarized epithelium. *J. Cell Sci.* **95**, 137–152 (1990).

50. L. G. Edgar, Blastomere Culture and Analysis. *Methods Cell Biol.* **48**, 303–321 (1995).

51. E. Schierenberg, B. Junkersdorf, The role of eggshell and underlying vitelline membrane for normal pattern formation in the early C. elegans embryo. *Roux's Arch. Dev. Biol.* **202**, 10–16 (1992).

52. J. Kim, *et al.*, Evaluation of morphokinetic characteristics of zona pellucida free mouse pre-implantation embryos using time-lapse monitoring system. *Int. J. Dev. Biol.* **64**, 415–422 (2020).

53. J.-L. Maître, R. Niwayama, H. Turlier, F. Nédélec, T. Hiiragi, Pulsatile cell-autonomous contractility drives compaction in the mouse embryo. *Nat. Cell Biol.* **17**, 849–855 (2015).

54. M. Takeichi, The cadherins : cell-cell adhesion molecules controlling animal morphogenesis. **655** (1988).

55. R. W. Style, *et al.*, Traction force microscopy in physics and biology. *Soft Matter* **10**, 4047–4055 (2014).

56. J. M. Belmonte, *et al.*, Virtual-tissue computer simulations define the roles of cell

adhesion and proliferation in the onset of kidney cystic disease. *Mol. Biol. Cell* **27**, 3673–3685 (2016).

57. H. Honda, T. Nagai, M. Tanemura, Two different mechanisms of planar cell intercalation leading to tissue elongation. *Dev. Dyn.* **237**, 1826–1836 (2008).

58. N. C. Rivron, *et al.*, Blastocyst-like structures generated solely from stem cells. *Nature* **557**, 106–111 (2018).

59. D. Serra, *et al.*, Self-organization and symmetry breaking in intestinal organoid development. *Nature* **569**, 66–72 (2019).

60. D. Drasdo, S. Höhme, A single-cell-based model of tumor growth in vitro: monolayers and spheroids. *Phys. Biol.* **2**, 133–147 (2005).

61. P. Vitorino, M. Hammer, J. Kim, T. Meyer, A Steering Model of Endothelial Sheet Migration Recapitulates Monolayer Integrity and Directed Collective Migration. *Mol. Cell. Biol.* **31**, 342–350 (2011).

62. M. Smutny, *et al.*, Friction forces position the neural anlage. *Nat. Cell Biol.* **19**, 306–317 (2017).

63. R. Montesano, G. Schaller, L. Orci, Induction of epithelial tubular morphogenesis in vitro by fibroblast-derived soluble factors. *Cell* **66**, 697–711 (1991).

64. H. Koyama, *et al.*, Mechanical Regulation of Three-Dimensional Epithelial Fold Pattern Formation in the Mouse Oviduct. *Biophys. J.* **111**, 650–665 (2016).

65. M. Eiraku, *et al.*, Self-organizing optic-cup morphogenesis in three-dimensional culture. *Nature* **472**, 51–6 (2011).

66. L. Solnica-krezel, D. S. Sepich, Gastrulation: Making and Shaping Germ Layers. *Annu. Rev. Cell Dev. Biol.* **28**, 687–717 (2012).

67. H. Honda, N. Motosugi, T. Nagai, M. Tanemura, T. Hiiragi, Computer simulation of emerging asymmetry in the mouse blastocyst. *Development* **135**, 1407–1414 (2008).

68. M. Nonomura, Study on multicellular systems using a phase field model. *PLoS One* **7**, 1–9 (2012).

69. B. A. Camley, *et al.*, Polarity mechanisms such as contact inhibition of locomotion regulate persistent rotational motion of mammalian cells on micropatterns. *Proc. Natl. Acad. Sci. U. S. A.* **111**, 14770–14775 (2014).

70. A. Kajita, M. Yamamura, Y. Kohara, Computer simulation of the cellular arrangement using physical model in early cleavage of the nematode Caenorhabditis elegans. *Bioinformatics* **19**, 704–716 (2003).

71. S. Ishihara, K. Sugimura, Bayesian inference of force dynamics during

morphogenesis. *J. Theor. Biol.* **313**, 201–211 (2012).

72. D. T. Tambe, *et al.*, Collective cell guidance by cooperative intercellular forces. *Nat. Mater.* **10**, 469–75 (2011).

73. S. B. Nissen, *et al.*, Four simple rules that are sufficient to generate the mammalian blastocyst. *PLoS Biol.* **15**, e2000737 (2017).

Figures

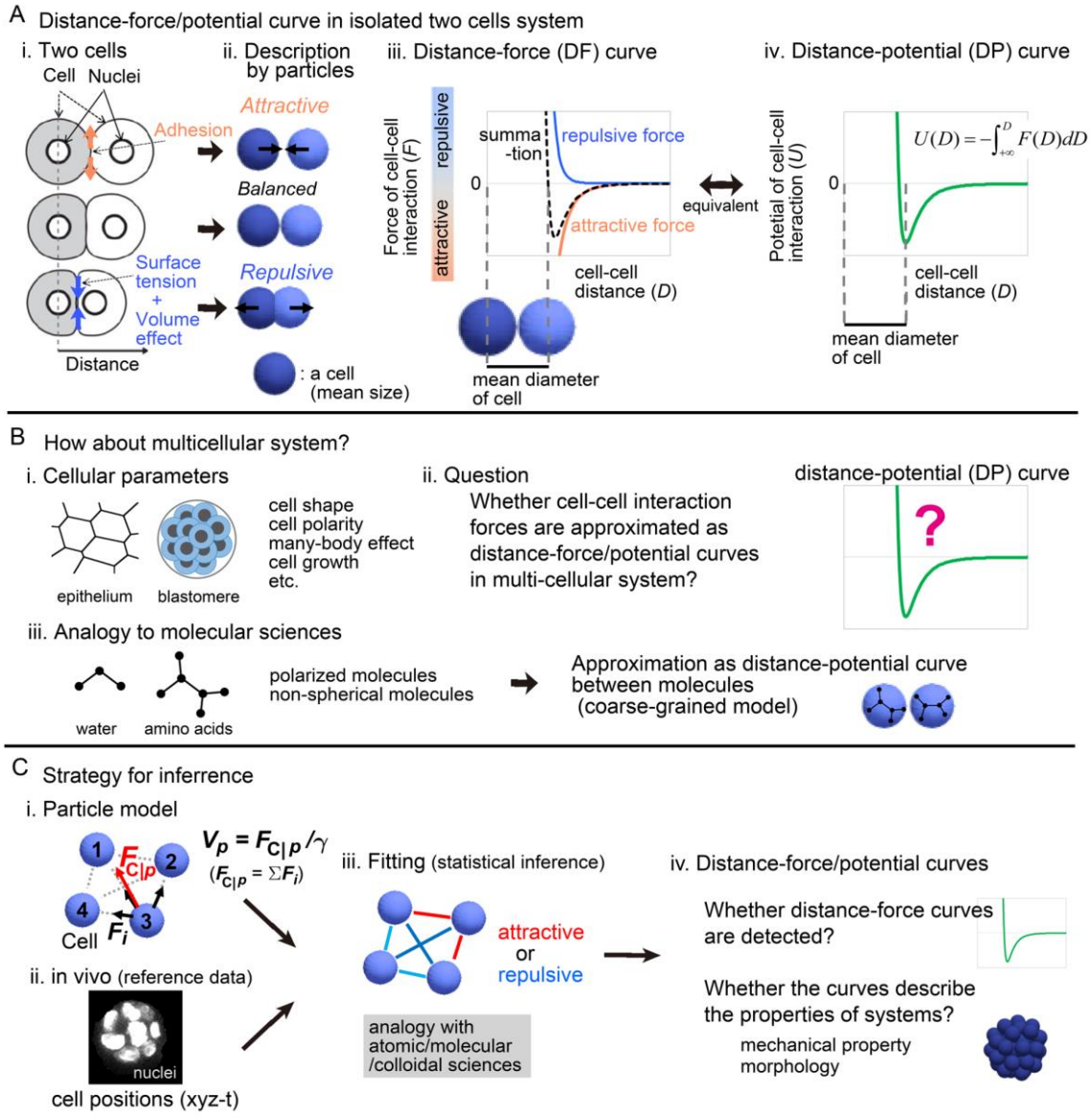

Figure 1: Overview of strategy for inferring the effective potential of cell–cell interactions A. Relationship between microscopic forces and attractive/repulsive forces in isolated two cell systems. i) Microscopic forces contributing to cell–cell interactions are exemplified. ii) The microscopic forces are approximated as attractive/repulsive forces where cells are described as particles with the mean size. iii) Both the repulsive and attractive forces are provided as cell–cell distance-dependent functions, and the

938 summation (black broken line) is the distance–force curve of the two particles. The
939 relationship between the curve and the mean diameters of the cells is shown. iv) A
940 distance–potential curve is shown where the mean diameters of cells correspond to the
941 distance at the potential minimum.

942 B. Approximation of cell–cell interaction forces in multicellular systems. i) Mechanical
943 parameters are exemplified. ii) The question in this study. iii) Approximation of particle–
944 particle interactions in molecular sciences.

945 C. Strategy for inferring effective forces of cell–cell interactions. i) Particle model. A blue
946 sphere corresponds to a cell. Attractive or repulsive force between the particles (blue
947 spheres #1–4), was considered; vectors of cell–cell interaction forces (F_i) are illustrated
948 by black arrows in the case of particle #3. The net force ($F_{C|p}$) of particle #3 is shown by
949 a red vector. The summation of F_i results in $F_{C|p}$ which determines the velocity ($V_{C|p}$) of
950 *p*th particle. ii) Nuclear tracking data were obtained and used as a reference data during
951 the inference. iii) Effective forces of cell–cell interactions were inferred by fitting. Red
952 line, attractive; blue line, repulsive. iv) From the inferred effective forces, we examined
953 whether distance–force curves are detected.

954 Related figure: Figure S1 (inference method).

955

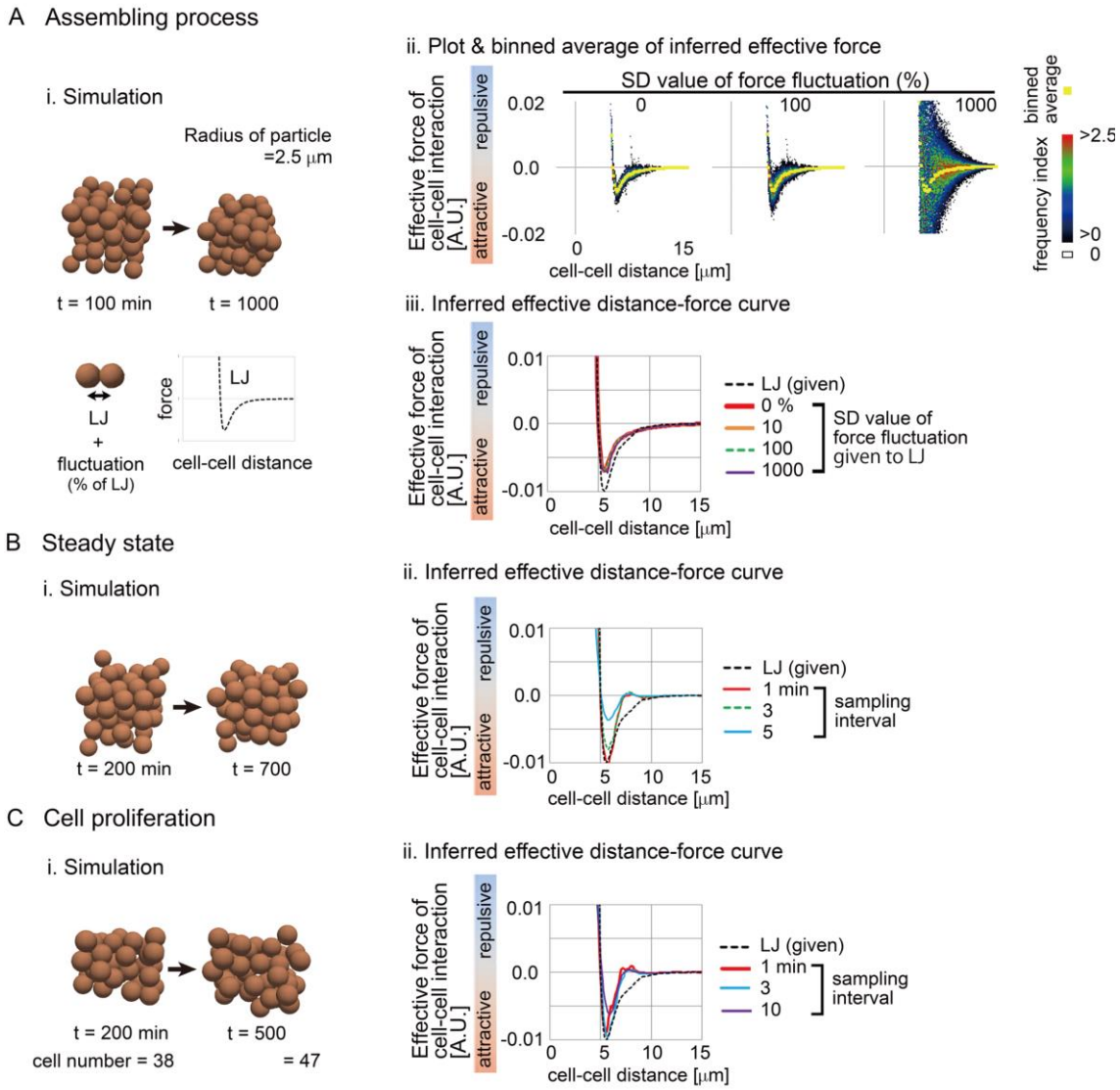

Figure 2: Validation of inference method using simulation data

Simulations were performed on the basis of a distance–force (DF) curve obtained from the Lenard-Jones potential (LJ). The DF curve is shown in A-i. The simulation conditions contain “Assembling process” (A), “Steady state” (B), and “Cell proliferation” (C). For A-C, snapshots of the simulations are shown where the particles are of the mean size of

963 cells (i). In A-ii, the procedure of data analyses is exemplified where effective forces of
964 interactions for each pair of cells for each time frame were plotted against the distance of
965 the cell–cell interactions, and shown as a colored heat map representing the frequencies
966 of the data points (Frequency index (FI)). Averaged values of the forces are shown in
967 yellow (binned average). In A-iii, B-ii, and C-ii, the resultant effective DF curves are
968 shown with the DF curves from the LJ potential.
969 Related figures: Figure S2 (in the case of other given potential and random walk).
970

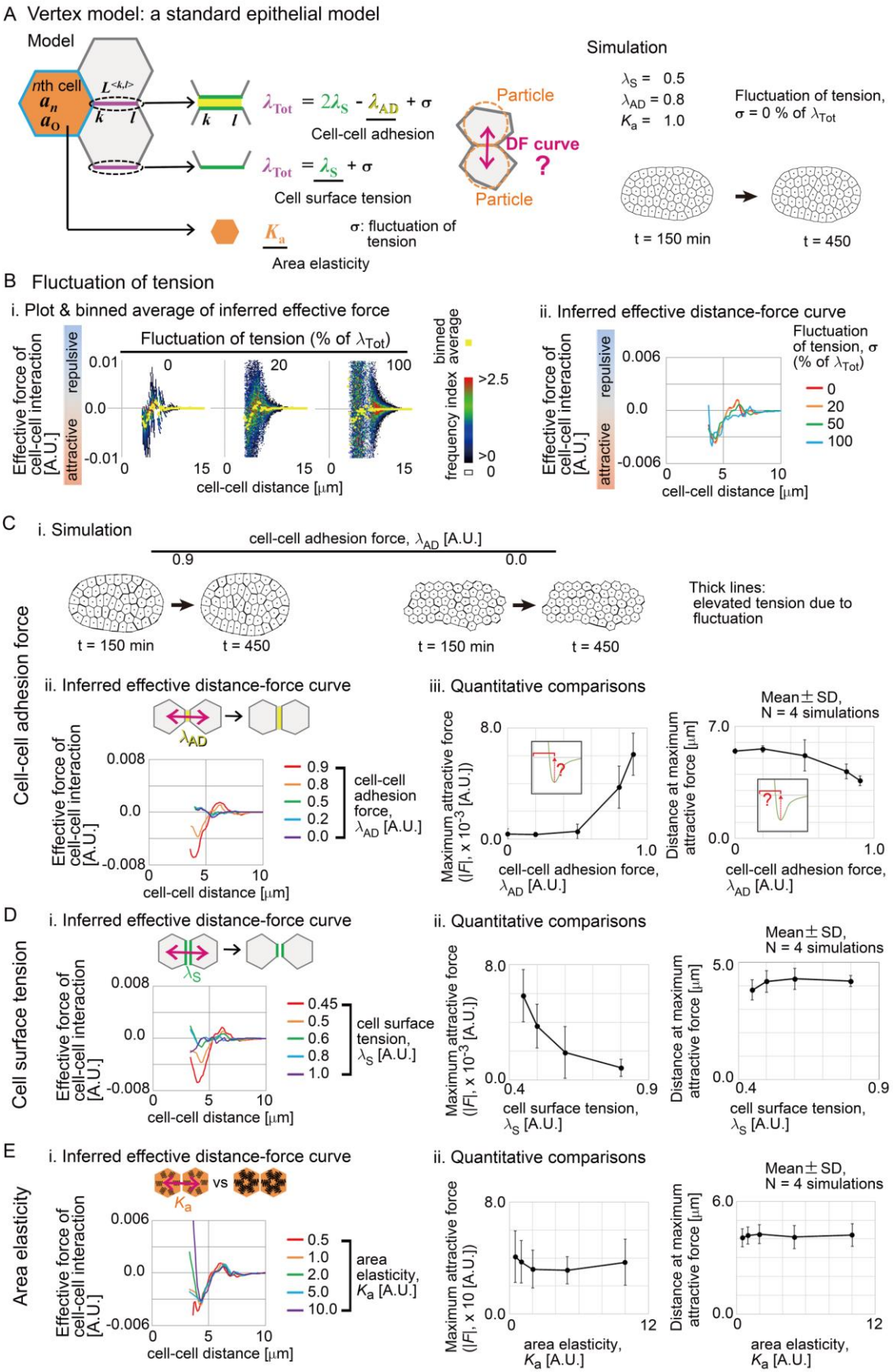
A Vertex model: a standard epithelial model
Model
nth cell
Cell-cell adhesion
Cell surface tension
σ: fluctuation of tension
Area elasticity
Particle
DF curve
Particle
Simulation
λS = 0.5
λAD = 0.8
Ka = 1.0
Fluctuation of tension, σ = 0 % of λTot
t = 150 min
t = 450
B Fluctuation of tension
i. Plot & binned average of inferred effective force
Fluctuation of tension (% of λTot)
Effective force of cell-cell interaction [A.U.]
repulsive
attractive
cell-cell distance [μm]
binned average
frequency index
ii. Inferred effective distance-force curve
Fluctuation of tension, σ (% of λTot)
C
i. Simulation
cell-cell adhesion force, λAD [A.U.]
Thick lines: elevated tension due to fluctuation
Cell-cell adhesion force
ii. Inferred effective distance-force curve
cell-cell adhesion force, λAD [A.U.]
iii. Quantitative comparisons
Mean ± SD, N = 4 simulations
Maximum attractive force (|F|, x 10-3 [A.U.])
Distance at maximum attractive force [μm]
D
Cell surface tension
i. Inferred effective distance-force curve
cell surface tension, λS [A.U.]
ii. Quantitative comparisons
E
Area elasticity
i. Inferred effective distance-force curve
area elasticity, Ka [A.U.]
ii. Quantitative comparisons

971

Figure 3: Inference of effective forces of cell–cell interaction in epithelial cell model

A. Vertex model. λ_{Tot} is the line tension exerted on cell–cell junctions or on cell edges of outer boundary. The potential energy on a junction or edge is $\lambda_{\mathrm{Tot}} L^{<k,l>}$, where L is the length of the junction or edge composed of kth and lth vertices. The potential energy for a cell provided by the area elasticity is $(1/2)K_{\mathrm{a}}\left(a_n / a_{\mathrm{o}} - 1\right)^2 a_{\mathrm{o}}$, where a_n is the area of nth cell and a_{o} is the natural area. An example of simulations is shown with the parameter values in the right panel.

B. Inferred effective distance–force (DF) curves under various values of the fluctuations of tension, σ. i) The inferred forces are plotted against cell–cell distances, and binned averages are show. ii) Inferred DF curves.

C. Inferred DF curves under various values of cell–cell adhesive forces, λ_{AD}. i) Simulation outcomes are shown where the cell cluster tends to form a circular colony under increased values of the adhesive forces (λ_{AD} = 0.9). ii) Inferred DF curves. iii) Quantitative comparisons of the DF curves.

D. Inferred DF curves under various values of cell surface tensions, λ_{S}. i) Inferred DF curves. ii) Quantitative comparisons of the DF curves.

E. Inferred DF curves under various values of area elasticities, K_{a}. i) Inferred DF curves. ii) Quantitative comparisons of the DF curves.

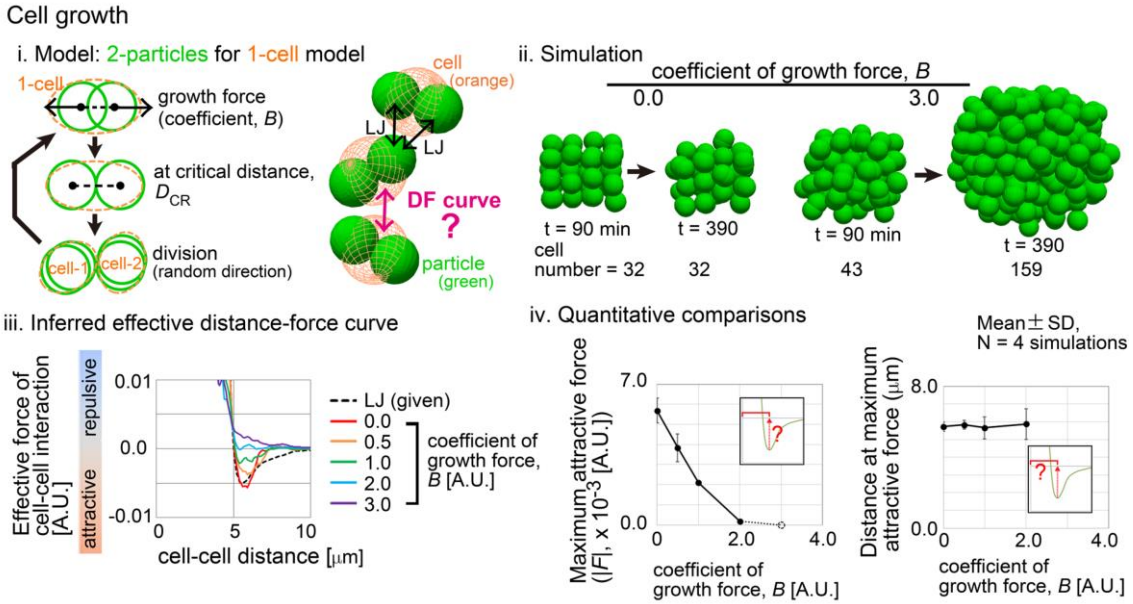

Figure 4: Inference of effective forces of cell–cell interaction in growing cells

i) Model of cell growth. Orange, a cell; green, particle. The growth force between the two particles is provided as a repulsive force as follows: $B/(D+C)^2$, $C = 5.6$. $D_{CR} = 5.0$. ii) Examples of simulations under different values of B, where the particles but not the cells are visualized. iii) Inferred DF curves. iv) Quantitative comparisons of the DF curves.

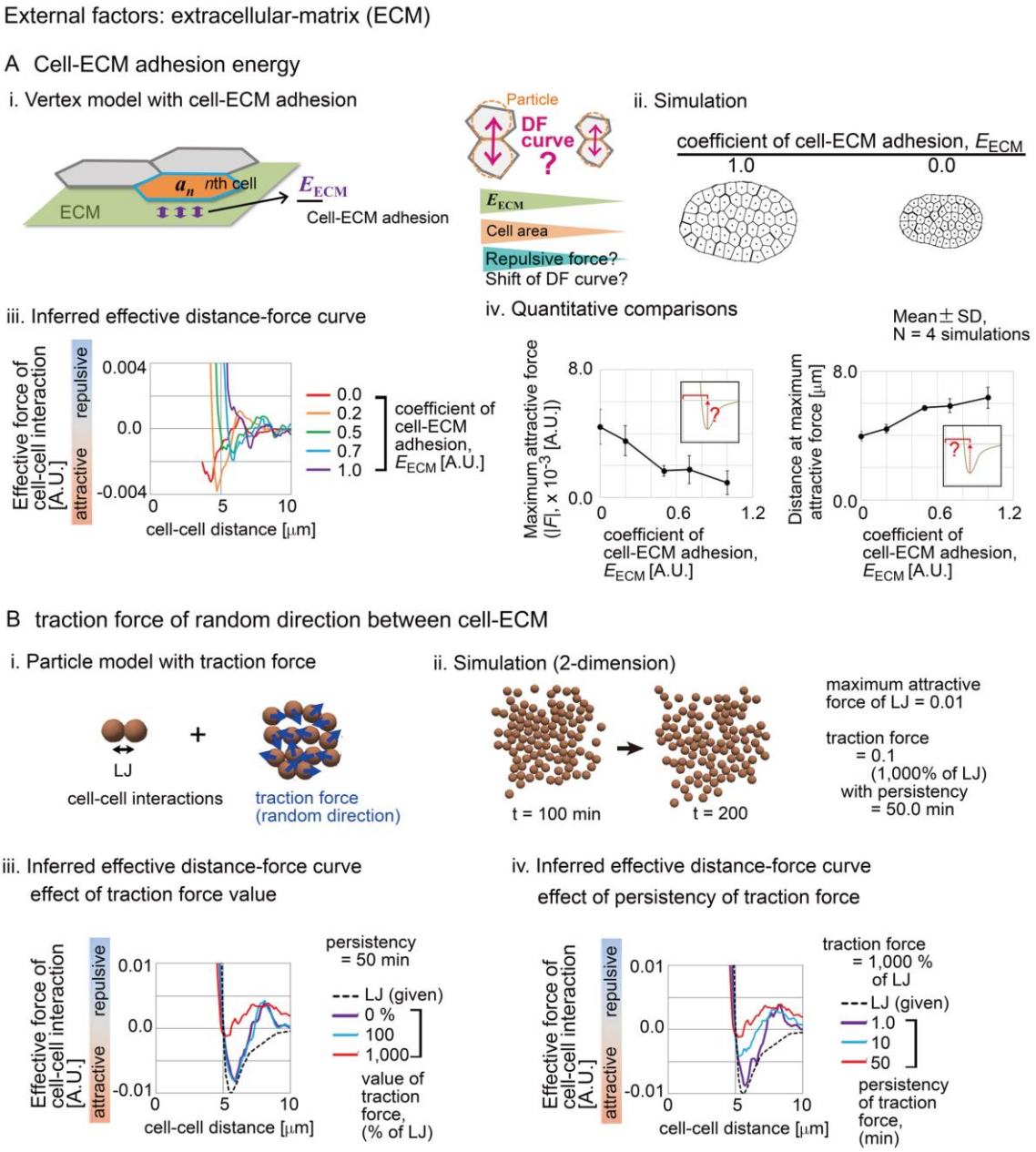

Figure 5: Influence of extracellular-matrix to effective forces of cell–cell interaction

A. Cell–ECM adhesion energy is assumed in the vertex model used in Fig. 3. i) The energy for a cell is defined as $-E_{\mathrm{ECM}}a_n$, where E_{ECM} is the coefficient of the energy. ii) Simulation outcomes are exemplified where the cell areas are increased under larger value of E_{ECM}. The left and right panels are shown with the same scale. iii) Inferred DF curves.

1005 iv) Quantitative comparisons of the DF curves.

1006 B. Traction forces between cells and ECM are assumed in the particle model used in Fig.

1007 2 except that the simulations were two-dimensionally performed. i) Cell–cell interaction

1008 forces are provided by the LJ potential. The directions of the traction forces are random.

1009 ii) An example of simulations is shown. iii and iv) Inferred DF curves under various

1010 values of the traction forces and under various values of the persistency, respectively.

1011 Related Figures: Figure S3 (inference in MDCK cells on substrates) and S4 (inference in

1012 migratory cells with a uniform direction) show a similar effect of migratory activities on

1013 DF curves to that in B.

1014

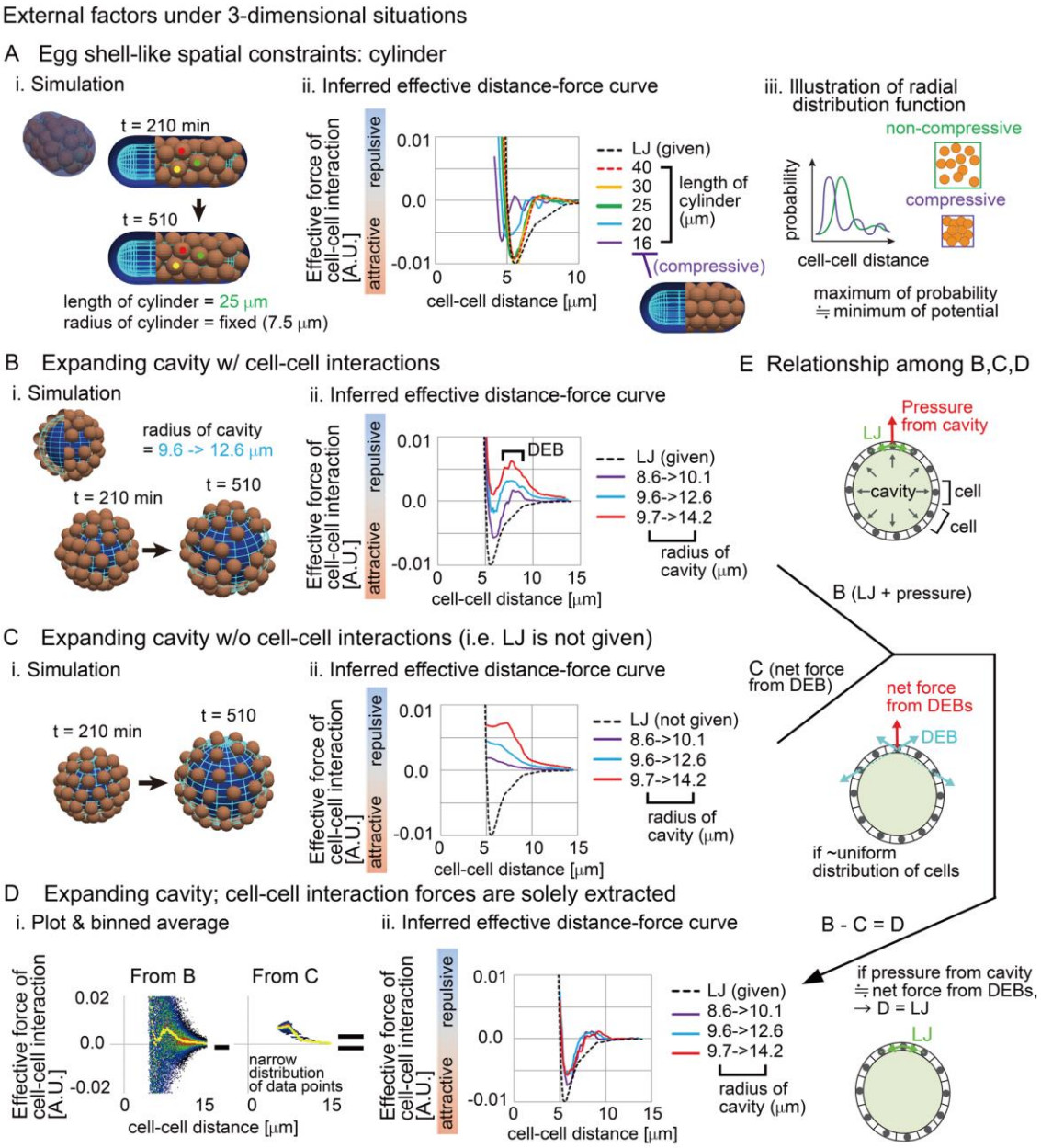

Figure 6: Influence of external constraints to effective forces of cell–cell interaction

A. Cylindrical constraints corresponding to egg shells are assumed in the particle model used in Fig. 2. i) An example of simulations with labeling three cells (red, yellow, and green). ii) Inferred DF curves. For the condition of the cylindrical length = 16μm, a snapshot of the simulation is shown ("compressive"). iii) Effect of compression on the

1021 radial distribution function is described. The functions under the compressive and non-
1022 compressive conditions are illustrated (purple and green lines). The maxima of the
1023 functions are expected to the minima of the effective potentials of cell–cell interactions.
1024 The numbers of the particles are the same among the different cylindrical constraints.
1025 B. Expanding cavities are assumed in the particle model. i) An example of simulations
1026 with the change in the radius of the cavity. ii) Inferred DF curves with the DEBs. The
1027 numbers of the particles are the same among the different cavities.
1028 C. Expanding cavities are assumed whereas cell–cell interaction forces are not introduced.
1029 i) An example of simulations. ii) Inferred DF curves.
1030 D. Reconstruction of cell–cell interaction forces under expanding cavities. i) All the data
1031 points in B and C under the radius of the cavity = 9.7 -> 14.2μm are plotted on distance–
1032 force graph with the binned averages. ii) DF curves obtained by subtracting the DF curves
1033 in C from those in B: i.e. B – C as exemplified in D-i.
1034 E. The subtraction performed in D is schematically explained in the relationship among
1035 B, C, and D.
1036 Related Figures: Figure S5 (inference under spherical constraints) and S6 (inference in
1037 cylindrical constraints) show a similar effect of spatial constraints on DF curves to that in
1038 A. Figure S7 (inference under non-expanding cavities) shows almost no modification of

DF curves.

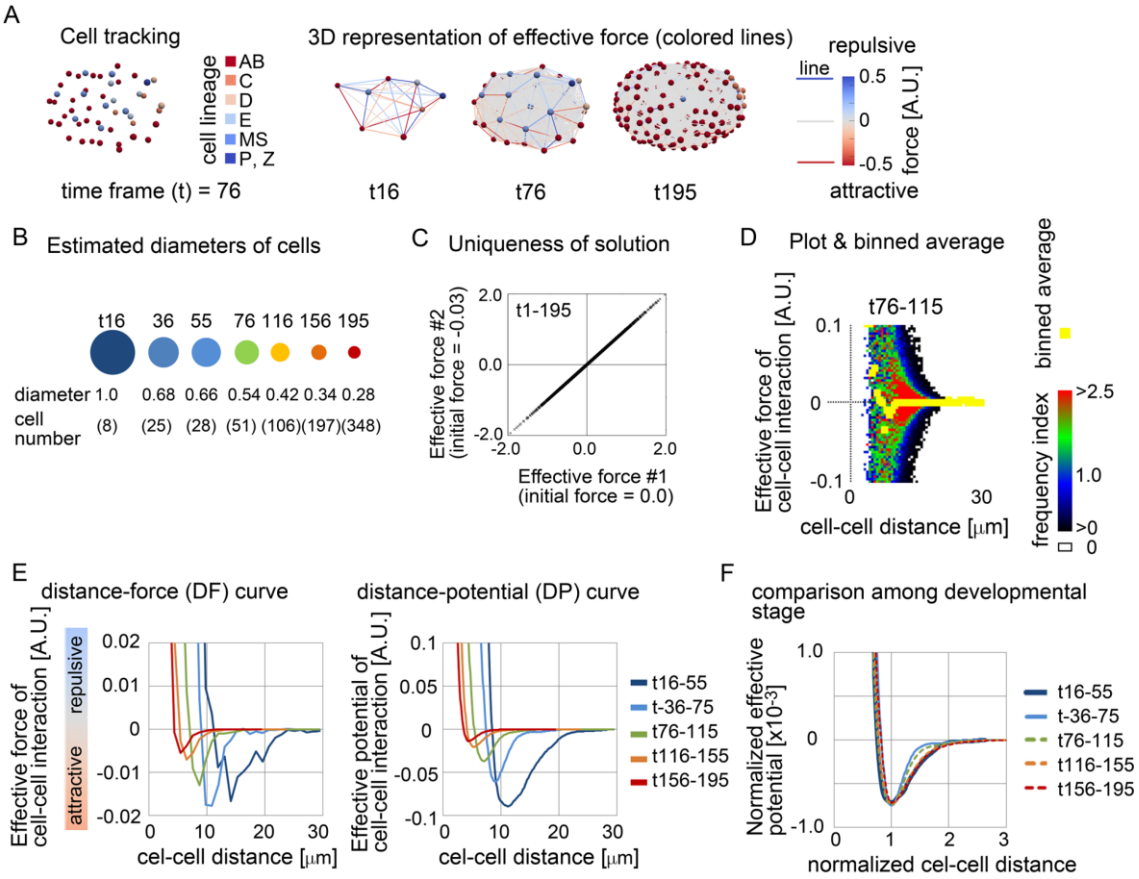

Figure 7: Inference of effective force of cell–cell interaction in *C.elegans* embryos

A. Snapshot of the nuclear positions in the *C.elegans* embryo with cell lineages at time frame = 76 in the left panel. Snapshots with inferred effective forces with the force values described coloed lines in right three panels at t = 16, 76, and 195. Forces are depicted in arbitrary units (A.U.); 1 A.U. of the force can move a particle at 1μm/min. The nuclear tracking data were obtained from a previous report (30).

B. Mean diameters of cells at each time frame estimated from cell numbers. Given that the volume of the embryos is constant (= *Vol*) during embryogenesis, the mean diameters were estimated from the cell numbers (N_c) at each time frame as follows: mean diameter

1053 $= \{Vol / (4/3\ \pi\ N_c)\}^{1/3}$. The diameters relative to that at time frame = 16 are shown with

1054 cell numbers. The sizes of the circles reflect the diameters, whose colors roughly

1055 correspond to the colors in the graph in E.

1056 C. Uniqueness of solution of effective force inference was examined. The minimizations

1057 of the cost function *G* were performed from different initial force values as described in

1058 the x- and y- axes, and the inferred values of each cell-cell interaction were plotted by

1059 crosses.

1060 D. The inferred effective forces of cell–cell interactions were plotted against the distance

1061 of cell–cell interactions with binned averages at t = 76-115.

1062 E. Inferred DF and DP curves at various time frames.

1063 F. DP curves normalized by the distances at the potential minima at various time frames.

1064 Related figure: Figure S8 (uniqueness of solution was examined).

1065 Related movies: Movie S1A (tracking data) and S1B (force map).

1066

1067

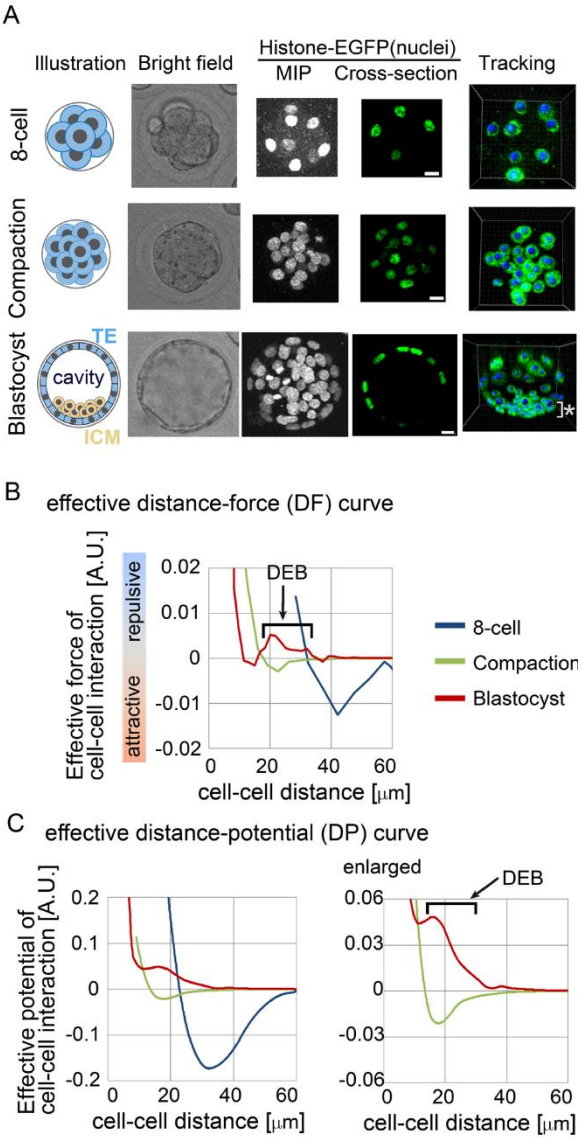

Figure 8: Inference of the effective force of cell–cell interaction in mouse pre-implantation embryos

A. Eight-cell, compaction, and blastocyst stages of mouse embryo are illustrated, and their confocal microscopic images are shown: bright field, maximum intensity projection (MIP) and cross-section of fluorescence of H2B-EGFP. Snapshots of nuclear tracking are also shown; blue spheres indicate the detected nuclei. In the nuclear tracking image of the blastocyst, ICM cells are located around the bottom region of the image, as indicated by *. Scale bars = 15μm.

B and C. Inferred DF and DP curves with the DEBs.

Related figures: Figure S9 (inference in cavitation-inhibited embryos), S10 (data from other embryos), and S11 (DF and DP curves in ICM and TE cells, and the outer and inner cells in the compaction stage).

Related movies: Movie S2A-C (tracking data) and Movie S2D-F (force maps)

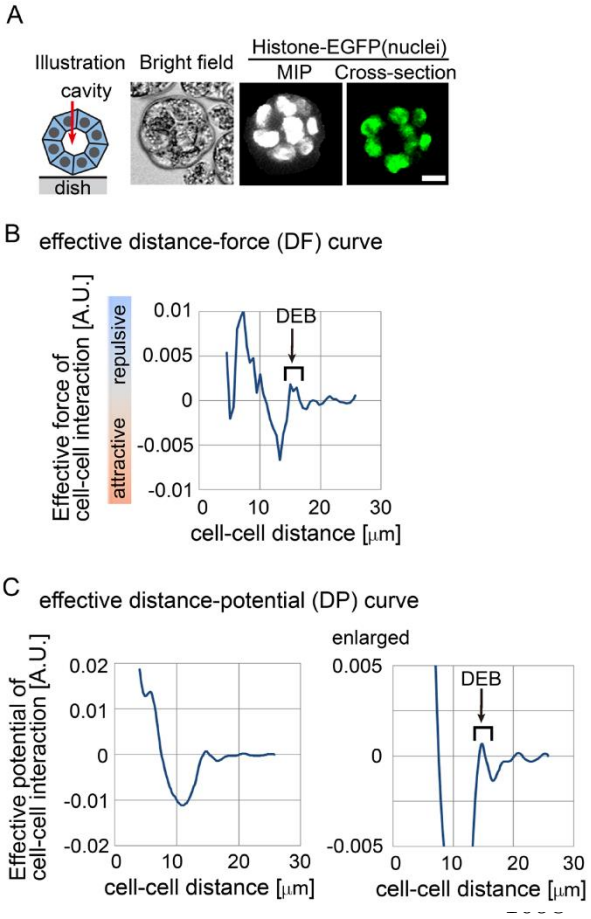

Figure 9: Inference of effective force of cell–cell interaction in cysts formed by MDCK cells

A. MDCK cysts formed under suspension conditions are illustrated, and confocal microscopic images are shown: bright field, maximum intensity projection (MIP) and cross-section of fluorescence of H2B-EGFP. Scale bars = 10μm.

B and C. Inferred DF and DP curves. In C, an enlarged view is also provided. A DEB is indicated.

Related figures: Figure S12 (all DP curves in other cysts show DEBs.).

Related movies: Movie S3A (tracking data) and Movie S3B (force maps)

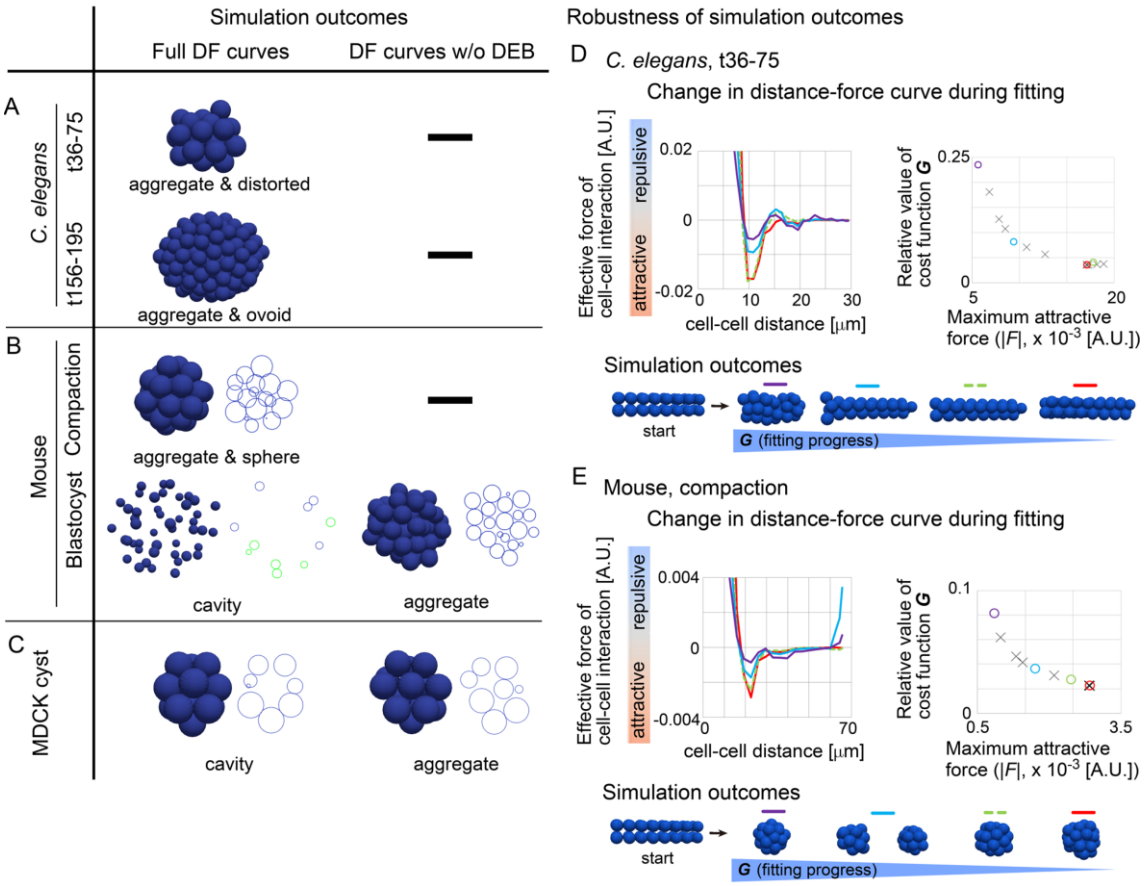

Figure 10: Outcomes of simulations based on inferred distance–force curves

A-C. Simulations results under the DF curves derived from *C. elegans* and mouse embryos, and the MDCK cyst are exemplified. In B and C, cross-sections are also shown. In the case of the mouse blastocyst, two parallel cross-sections (shown in blue and green) are merged.

D and E. DF curves sampled before reaching the minima of *G*, and simulation outcomes. DF curves, left panels; the values of *G* and the maximum attractive forces in the DF curves, right panels; simulation outcomes for each DF curve with the initial configuration ("start"), bottom panels. The values of *G* are relative to that in the case of all forces = 0.

The colors in each three panels in D and E correspond each other. In the right panels, the numbers of the data points are 14 and 12 in D and E, respectively, and the representative ones (colored circles) are selected for presenting the DF curves and the simulation outcomes.

Related figure: Figure S13 (other simulation results with initial configurations showed equivalent results in Fig. 10A-C).

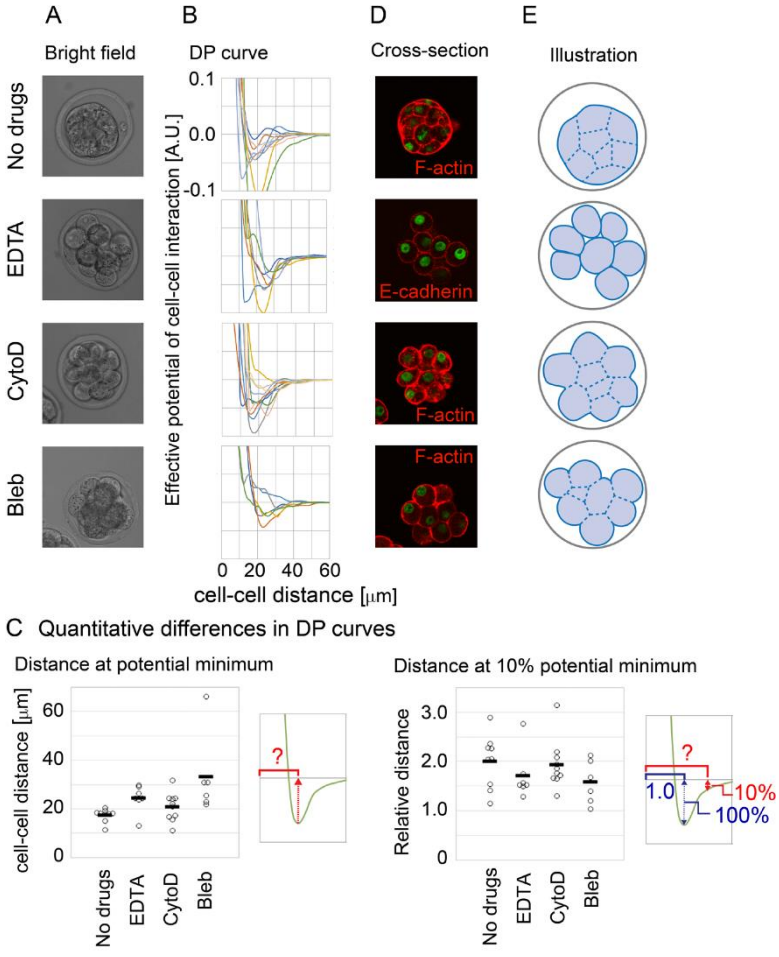

Figure 11: Inference of effective potentials of cell–cell interaction in compaction-inhibited mouse embryos

A. Microscopic images of embryos under chemicals. CytoD, cytochalasin D; Bleb, blebbistatin.

B. Inferred DP curves in the drug-treated embryos. N=6~10 for each condition.

C. Quantitative differences in the DP curves. Distances at the potential minima in the DP curves, left panel; Distances providing 10% energy of the potential minima as the relative value to the distances at the potential minima, right panel. Mann–Whitney–Wilcoxon tests

1132 were performed and the resultant *p*-values for “No Drugs” vs. “EDTA”, vs. “CytoD”, and

1133 vs. “Bleb” are 0.011, 0.23, and 0.00040, respectively, in the left panel. In the right panel,

1134 distances providing other % energies instead of 10% are shown in Fig. S16B.

1135 D. Confocal microscopic images of cell shapes. Cell shapes were visualized by staining

1136 F-actin or E-cadherin. E. The embryonic and cellular shapes illustrated based on D.

1137 Related figures: Figure S14 (experimental design), S15 (enlarged view of DP curves),

1138 S16 (details of quantification of DP curves), and S17 (histological images of other

1139 embryos).

1140

1141

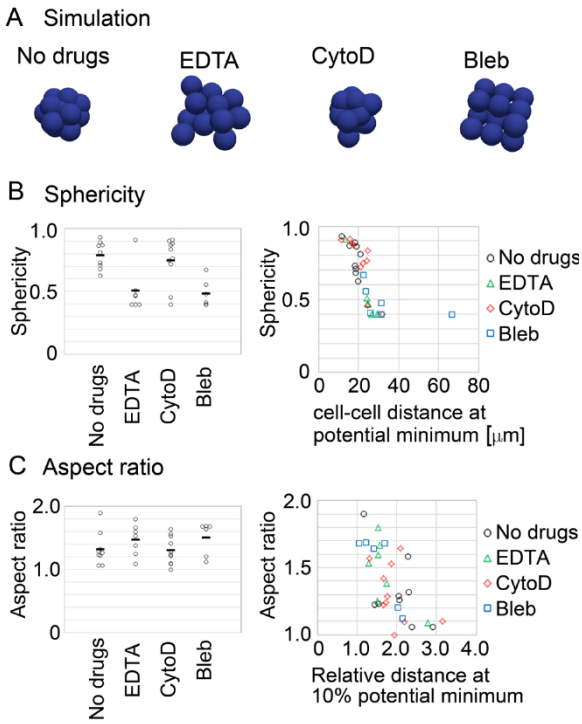

Figure 12: Simulations under inferred distance–potential curves in drug-treated embryos, and identification of parameters explaining morphological transition

A. Simulation results for the drug-treated embryos. All simulation data are provided in Figure S18, and the representative results which nearly showed the mean values of the sphericities for each condition are chosen here.

B. Sphericities in the simulations of the drug-treated embryos (left panel), and the sphericities plotted against the distances at the potential minima calculated in Figure 11C. Mann–Whitney–Wilcoxon tests were performed: *p*-values for “No Drugs” vs. “EDTA”, vs. “CytoD”, and vs. “Bleb” are 0.011, 1.0, and 0.00080, respectively.

C. Aspect ratios in simulations of the drug-treated embryos (left panel), and the aspect ratios plotted against the relative distances providing 10% energy of the potential minima calculated in Figure 11C. Mann–Whitney–Wilcoxon tests were performed: *p*-values for “No Drugs” vs. “EDTA”, vs. “CytoD”, and vs. “Bleb” are 0.21, 0.97, and 0.33,

respectively.

Related figures: Figure S18 (all simulation outcomes), S19 (sphericities and aspect ratios from a different initial configuration), and S20 (Relationships of sphericities or aspect ratios to other tested parameters).

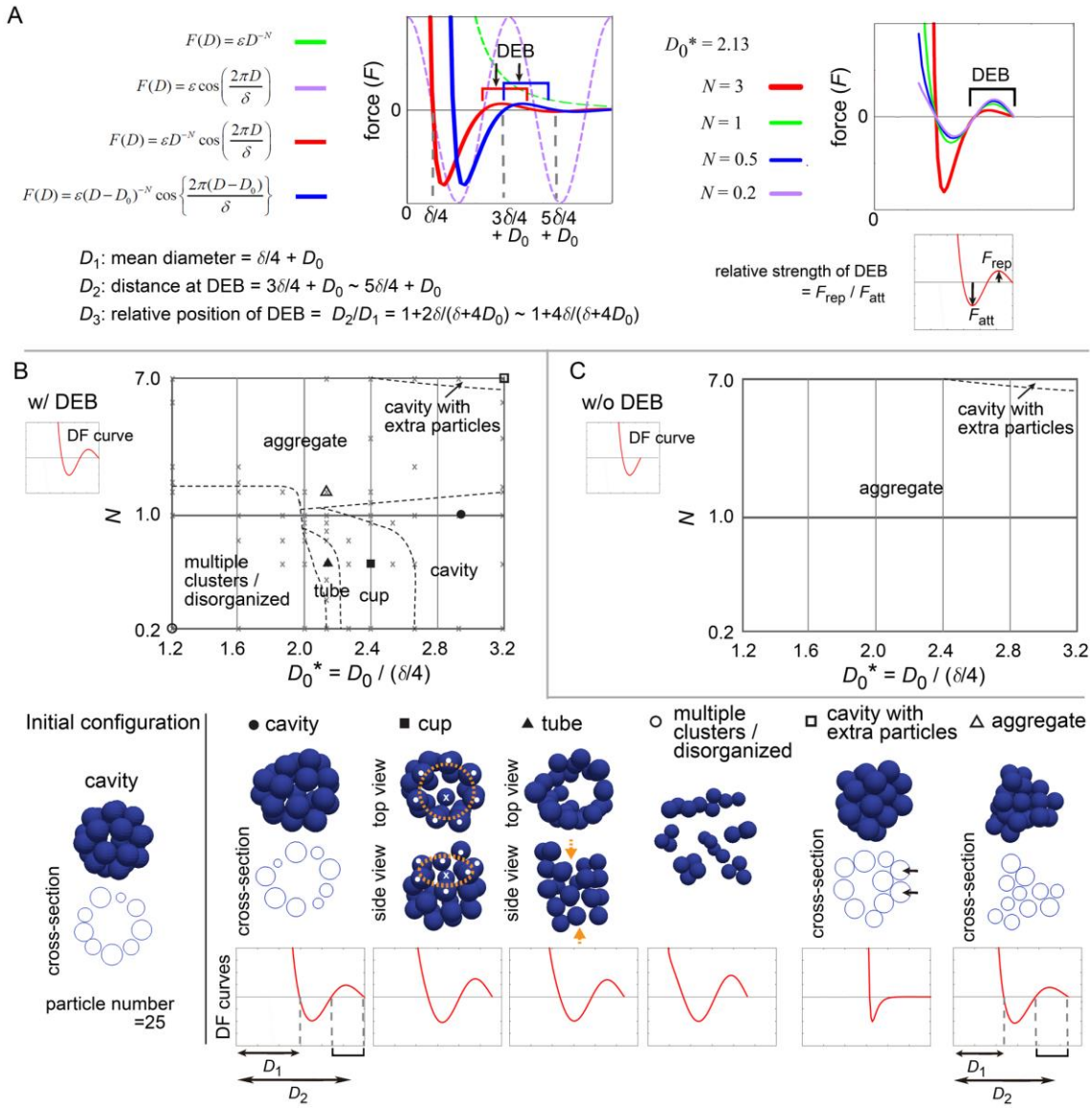

Figure 13: Modeling of distance–force curves and diagrams of simulation outcomes; cavity-bearing structures

A. Modeling of DF curves using four parameters: N, D_0, δ, and ε. A DF curve without the cosine term is always >0 (repulsive) ($F = \varepsilon D^{-N}$, green broken line). Upon introduction of the cosine (purple broken line), the curves acquire regions with <0 (attractive) and a DEB (red line). Upon introduction of D_0, the curves are translated along the distance (blue line).

As shown in the blue line, the DEB ranges from $3\delta/4+D_0$ to $5\delta/4+D_0$ (D_2). N affects the gradient of the curves and the height of DEBs (right panel). DF curves from $D = 0$ to D at the end of DEBs (w/ DEB) or the curves from $D = 0$ to D before starting DEB (w/o DEB) were used in the following simulations.

B. Outcomes of simulations under various values of N and D^*. Some conditions on the diagram were designated by symbols (circle, square, and triangle), and their simulation results are visualized (blue spheres) with the profiles of the DF curves. Cross-sections are visualized for some simulation results. The diameters of the blue spheres are equivalent to the mean diameter. For "cup" [orange rings, mouth of the cup; white dots, particles located on the ring; crosses, the particles located neither on the ring nor at the center of the ring]. For "tube" [orange crosses, open ends of the tube]. For "cavity with extra particles" [arrows, extra particles where multiple- but not single-layered]. D_1, mean diameter; D_2, distance of DEBs. The definition of each phase is explained in SI (section 7-2). Gray crosses, data points for depicting the lines separating each phase.

C. Simulation outcomes without DEBs.

Related figure: Figure S21 (phase diagrams under a different number of particles), S22 (maintenance of tubes was examined under DF curves with DEBs).

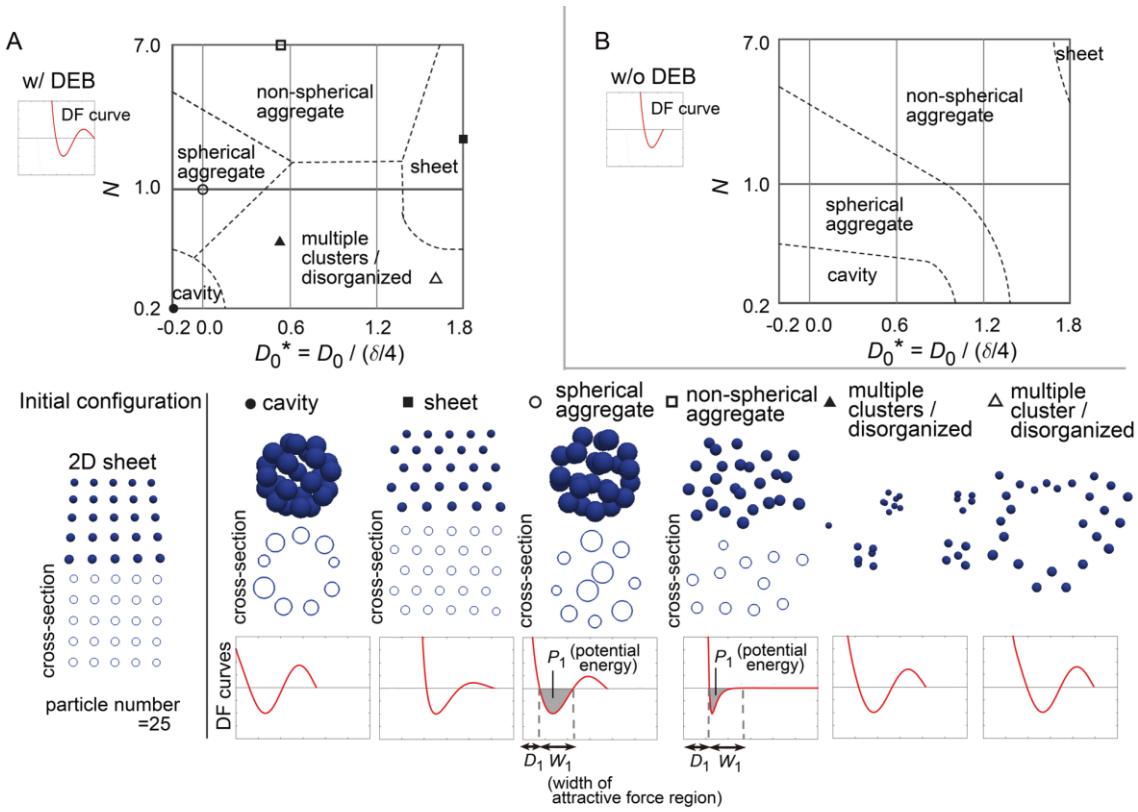

Figure 14: Diagrams of simulation outcomes; 2D sheets, spherical/non-spherical aggregates

A. Outcomes of simulations starting from a two-dimensional (2D) sheet with slight positional fluctuations. The results are shown in a similar manner to Fig. 13B, except that the diameters of the blue spheres are equivalent to 0.4× the mean diameter. D_1, mean diameter; W_1, width of attractive force regions; P_1, potential energy derived from attractive forces.

B. Simulation outcomes without DEBs.

Related movie: Movie S4 (2D sheets were stably maintained under fluctuations).

Table: effect of cellular and external factors on effective force of cell-cell interaction

	Effect on force (attractive or repulsive)	Effect on distance at maximum attractive force	Others	Figures
Cellular factors				
cell-cell adhesion	attractive	N.C.		3C
cell surface tension	repulsive	N.C.		3D
area elasticity	neutral	N.C.	core stiffness increased?	3E
cell growth	repulsive	N.C.		4
External factors				
cell-ECM adhesion	repulsive	increased		5A
cell-ECM traction force				
i. random direction	neutral/repulsive	N.C.		5B
ii. uniform	neutral	N.C.		S4A
iii. leader cells	repulsive	N.C.		S4B
egg-shell	neutral	N.C.	shift of DF curve under compresssive condition (non-physiological)	6A,S5,S6
cavity				
i. expanding	repulsive	N.C.	DEB generated	6B
ii. non-expanding	neutral	N.C.		S7

N.C; not changed